Seasonal Variability of Freshwater Plumes in the Eastern Gulf of Guinea as Inferred From Satellite Measurements

O. J. Houndegnonto[1] , N. Kolodziejczyk[1] , C. Maes[1] , B. Bourlès[2] , C. Y. Da-Allada[3,4,5] , and N. Reul[1]

[1]University of Brest, IRD, CNRS, Ifremer, Laboratoire d'Océanographie Physique et Spatiale (LOPS, UMR 6523), Brest, France, [2]US IMAGO (IRD), Brest, France, [3]LaGEA/ENSTP/UNSTIM, Abomey, Benin, [4]ICMPA-UNESCO Chair/UAC, Cotonou, Benin, [5]LHMC/IRHOB, Cotonou, Benin

Abstract In the eastern Gulf of Guinea (GG), freshwater originated from rivers discharges into the ocean and high precipitation rate are key contributors to the upper ocean vertical density stratification, and play a key role in modulating local air-sea interactions as well as biogeochemical cycle. Nevertheless, the dynamics of the GG freshwater plumes remain poorly documented because of the scarcity of historical, in situ observations and the lack of an ad hoc satellite-based analysis in this region. Recent advances in remote sensing capabilities from the Soil Moisture and Ocean Salinity (SMOS) satellite mission offer unprecedented coverage and spatiotemporal resolution of Sea Surface Salinity (SSS) in the GG. Using SMOS SSS and available in situ measurements, the seasonal variability of freshwater plumes and associated physical mechanisms controlling their seasonal cycle are presented and analyzed. Freshwater plumes in the GG follow two dynamical regimes. They present maximum offshore extension during boreal winter and exhibit minimum signature during summer. In the northeastern GG, SSS variability is mainly explained by high precipitation rate and Niger River runoff during winter, while during late summer, SSS is mainly driven by horizontal advection. In contrast, southeast of GG, freshwater plumes are mainly supplied by Congo River runoff. From September to March, SSS variability is driven by zonal advection, with a major contribution from Ekman wind-driven currents. During spring-summer, the observed SSS increase is likely explained by entrainment and vertical mixing. SSS budget and freshwater advection processes are discussed in the context of the shallow stratification induced by freshwater.

Plain Language Summary The Gulf of Guinea (GG) receives a large amount of freshwater from Congo and Niger rivers runoff and high precipitation. Since the freshwater is lighter than the seawater, the surface freshwater input is spread within large plumes that impact the upper layer vertical structure. The vertical stratification induced by the freshwater plume strongly impacts the air-sea heat flux exchanges but also the vertical exchanges of nutrient and organic matter. The eastern GG freshwater plumes remain poorly documented because of the scarcity of historical data in this region. This study, based on recent advancements in remote sensing of the Sea Surface Salinity from the European Space Agency Soil Moisture and Ocean Salinity satellite mission, provides a robust characterization of seasonal variability of freshwater plumes in the eastern GG by describing and quantifying their development, extent and dispersal patterns. The freshwater plumes are mainly supplied by rain (respectively river) input in the northern (respectively southern) part of this region. Their offshore seasonal evolution is mostly driven by surface currents and upward salty water fluxes. Surface wind-driven currents are also found to play a major role in the freshwater plumes offshore extension.

1. Introduction

The eastern Gulf of Guinea (GG) is characterized by an intense water cycle sustained by heavy precipitation due to seasonal cycle of the Inter-Tropical Convergence Zone (ITCZ) (Boisvert, 1967; Brandt et al., 2011; Diakhaté et al., 2016), and by strong land-sea exchanges through several rivers discharges, notoriously the two largest hydrographic basin runoffs in the GG: that is, Niger River, which discharges in a delta, and the Congo River, the second largest river discharge in the world. The river runoffs are sources of turbidity, organic and inorganic particles, nutrients, and sediments with suspended matter, which support geochemical and biological cycles of the upper trophic system (Brando et al., 2015; Dogliotti et al., 2016; Fournier et al., 2015; Vieira et al., 2020), and significantly impact fishery, a key socio-economical activity for the region. Rivers

freshwater inputs also modify the upper ocean thermohaline properties (salinity and temperature), and thus the buoyancy and vertical stratification of the surface layers. Strong vertical salinity gradients associated with fresh pools are generally found in the upper layer of the tropical oceans (e.g., Alory et al., 2012; Cole et al., 2015; de Boyer Montégut et al., 2014; Dossa et al., 2019; Durand et al., 2019; Kang et al., 2013; Maes & O'Kane, 2014; Materia et al., 2012; Pailler et al., 1999; Reul, Quilfen, et al., 2014). Rivers runoffs can shallow the mixed layer depth (MLD), by limiting or preventing vertical mixing between the upper warm layer and the cold ocean interior, through the so-called barrier layer mechanism. The barrier layer allows temperature inversion at the base of MLD and modulates air-sea interactions (Balaguru et al., 2012; Foltz & McPhaden, 2009; Mignot et al, 2007, 2009, 2012; Sprintall & Tomczak, 1992; Varona et al., 2019). Accordingly, seasonal to interannual air-sea interactions as well as regional climate could be affected by the variability of the upper ocean freshwater content in the region (Mignot et al., 2012; Reul, Quilfen, et al., 2014).

Freshwater inputs could also affect the ocean surface current structures and velocities due to the generation of anomalous buoyant plumes (Soloviev et al., 2002). For example, from a numerical model experiment, Varona et al. (2019) showed that the Amazon River discharge strongly affects the North Equatorial Counter Current (NECC) velocities. At smaller scale and within coastal band (<50 km), Horner-Devine et al. (2015) reported that knowing the structure of freshwater plumes pathways is essential for identifying the overall fate and transport of the freshwater discharge, as well as any nutrients, pollutants, sediments carried out by the plume. Hence, it is crucial to monitor the spatial extent and the dispersal pattern of freshwater plumes to better understand the upper ocean dynamics within these fresh buoyant plumes, especially in the GG.

Colored Dissolved Organic Matter (CDOM) and Turbidity (T_u) by Sediments (S_{ed}) and suspended matter (S_{mat}) and low Sea Surface Salinity (SSS) patterns are ubiquitous indicators of the river plumes (e.g., Brando et al., 2015; Constantin et al., 2016; Dogliotti et al., 2016; Falcini et al., 2012; Fournier et al., 2015; Schroeder et al., 2012). Detecting freshwater plumes by these former indicators (CDOM, T_u, $S_{ed,}$ and S_{mat}) are usually based on the upper water column optical properties such as the absorption coefficient of colored detrital matter (a_{cdm}), light penetration, and reflectance. Their measurement by satellite are however strongly contaminated by cloud coverage or other optically active substances that absorb almost in the nearest/same waveband such as chlorophyll-a concentration resulting from coastal upwelling processes (e.g., Hopkins et al., 2013). Hence, due to the dilution effect of freshwater on seawater salinity, the SSS is the best tracer of freshwater plumes variability from coastal to basin-scale dynamics.

From numerical modeling experiments dedicated to the eastern GG basin, Berger et al. (2014) showed that both precipitation and rivers runoffs are necessary to explain permanent low SSS values in the Bight of Biafra. On the other hand, they also showed that the Congo River discharge alone can explain most of the low SSS patterns south of the equator (see also Camara et al., 2015; Tzortzi et al., 2013; Yu, 2011). Nonetheless, the dispersal patterns and physical processes responsible for the freshwater plumes variability remain poorly documented, mainly because of the scarcity of historical in situ observations in this particular region. Our knowledge on the river plumes variability and their impacts on the ocean dynamics in this region mostly relies on the few observational studies conducted since the 1960s (Berrit & Donguy, 1964; Boyer & Levitus, 2002; Dessier & Donguy, 1994; Eisma & Kalf, 1984; Eisma & Van Bennekom, 1978; Materia et al., 2012; Meulenbergh, 1968; Reverdin et al., 2007). By combining available in situ observations and numerical model results, Da-Allada et al. (2013) analyzed the mixed layer salinity (MLS) budget in the whole tropical Atlantic. However, they found large uncertainties in the SSS budget established for the river plume areas in the eastern GG due to the sparseness of in situ data.

Recent advances in SSS remote sensing capabilities using L-Band microwaves sensors on the European Space Agency (ESA) Soil Moisture and Ocean Salinity (SMOS), the NASA Aquarius, and the NASA Soil Moisture Active Passive (SMAP) satellites missions now offer unprecedented spatio-temporal resolution of the tropical SSS fields (Reul et al., 2020), with an average resolution of 45×45 km^2 and a revisit time of 4 days (for SMOS and SMAP). The L-band satellite capability allows the monitoring of large mesoscale SSS features at unprecedented vicinity of the coast (~50 km). In the GG, several recent studies have used satellite SSS data to analyze the SSS spatio-temporal distribution in association with large river plumes from synoptic to interannual time scales (Chao et al., 2015; Hopkins et al., 2013; Reul, Fournier, et al., 2014). By using the data collected during the first year (2010) of the SMOS mission, Hopkins et al. (2013) presented a qualitative overview of freshwater plumes characteristics off Congo: the mean SSS distribution within the

freshwater plumes is found to change with the seasonal cycle of the Congo River discharge and to be correlated with the local wind stress. However, the potential role of ambient surface currents on the freshwater plumes seasonal variability remains unclear (Vic et al., 2014). From the first 3 years (2010–2012) of SMOS SSS data, Reul, Quilfen, et al. (2014) suggested that combining information on surface currents, rain rates, and SSS together with rivers discharges would allow to better quantify the variability of the hydrological cycle in the GG. Moreover, due to the shortness of the time series and near coastal contamination of the first releases of SMOS SSS products, a quantification of physical drivers of freshwater plumes variability remains to be done.

Recent improvements in SMOS data products have allowed to mitigate the coastal biases and filter out the SMOS satellite data contaminated by radio frequency interference (RFI), as well as conserving the strong SSS dynamics in the coastal region, especially within the river plumes (Boutin et al., 2018; Kolodziejczyk et al., 2016). More than one decade of SMOS SSS is now available, enabling us to monitor the seasonal and interannual SSS dynamics in the GG from regional to basin scales, including the near coastal ocean affected by river discharges. Furthermore, the increase of Argo profiling floats deployment, the yearly French PIRATA research cruises (Bourlès et al., 2019) and voluntary observing ships (VOS) have recently resulted in a consistent amount of in situ data in the eastern GG.

The present study aims are twofold. The first objective is to provide a refined characterization of the spatio-temporal variability of the freshwater plumes at seasonal scale by describing and quantifying their development, extent, and dispersal patterns based on the SMOS SSS data. The second objective is, by using estimates of the freshwater fluxes into the ocean (evaporation, precipitation, and runoffs) and surface currents from altimetry and in situ measurements, to quantify the physical processes involved in the SSS seasonal variability within two subregions of the GG: (1) off Congo (dashed black box: 5°E–13°E and 9°S–3°S, Figure 1c), and (2) off Niger River, the northeastern-most part of the GG (solid black box: 4°E–10°E and 0.5°N–6°N, Figure 1c). Indeed, freshwater plumes (induced by rivers runoff and/or precipitation) are fundamentally multiscale flow structures, which occur in a range of sizes and shapes, depending on the primary parameters that determine their dynamics: freshwater discharge, tidal amplitude, coastline bathymetry/geometry, ambient ocean currents and water properties, wind stress, and Earth's rotation (Horner-Devine et al., 2015). As SMOS SSS data are limited in the coastal scale, diagnostics of freshwater plumes dynamics in the range of estuaries to coastal scales is not the goal of the present study. Here, the dynamics of the freshwater plumes are analyzed by considering the regional scale of SSS dilution footprint due to rivers runoff and precipitations. We focus specifically on the dominant processes that contribute to the far-field dynamics of freshwater plumes at regional scale (Horner-Devine et al., 2015).

The study is organized as follows: data and methods are described in Sections 2 and 3; the major results are presented in Section 4; and Section 5 is dedicated to discussion and conclusion.

2. Data

2.1. SMOS SSS Observation and Validation

Launched in November 2009, the SMOS satellite is an ESA's Earth Explorer Opportunity mission dedicated to measure global Soil Moisture and Ocean Salinity (Kerr et al., 2010; Reul et al., 2020). This mission is part of the Living Planet Program which aims at monitoring Essential Climate Variables, such as the ocean's surface salinity (Mecklenburg et al., 2012). SMOS follows a sun-synchronous polar orbit with a local equator-crossing time at 6 a.m. for ascending passes and a repeat sub-cycle of about 18 days. SMOS is equipped with the MIRAS L-band (frequency of ~1.4 GHz) interferometric radiometer instrument providing SSS (retrieved from brightness temperature), with a ground resolution of about 50 km and a global coverage reached after 3–4 days. In this study, the so-called SMOS SSS CEC-LOCEAN L3 18 days debiased-V2.1 products are used. This product relies on improved outliers filtering (i.e., more efficient RFI contamination screening) and reduction of systematic biases to provide enhanced SSS accuracy along the coasts (Boutin et al., 2018; Kolodziejczyk et al., 2016). In this product, the noise has been reduced using an 18-day running Gaussian filtering and a 25-km median filter. The product is provided on 1/4° horizontal grid (EASE grid), with a 4-day time interval and covers the period 2010–2017. This product has been shown to be particularly
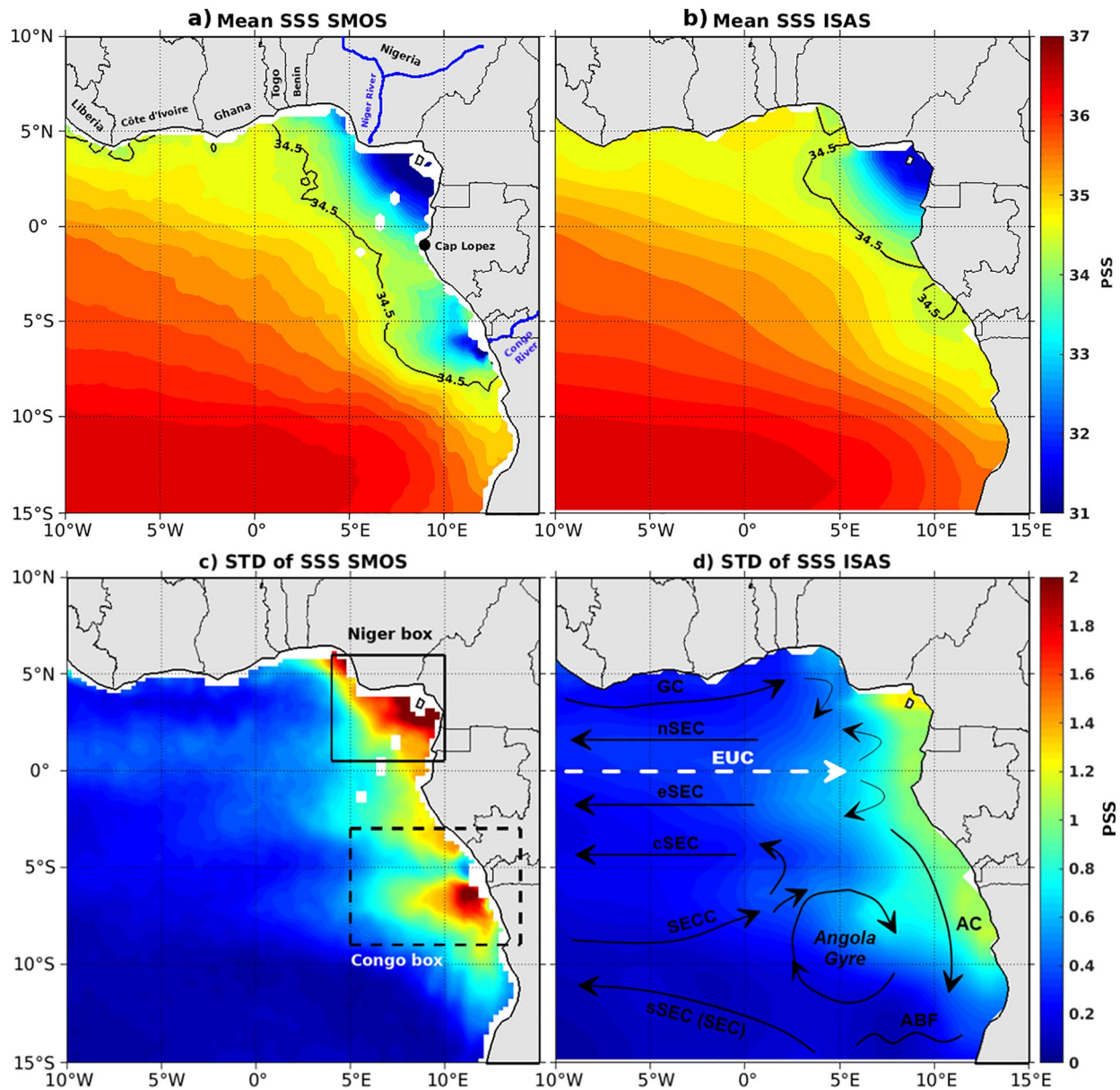
Figure 1. Map of the temporal mean SSS derived from (a) SMOS (2010–2017) and (b) ISAS (2010–2016). The bottom panels are the standard deviation of SSS seasonal cycle from (c) SMOS and (d) ISAS SSS in situ product. The solid black box and the dashed black box represent the Niger box (4°E–10°E and 0.5°N–6°N) and the Congo box (5°E–13°E and 3°S–9°S), respectively. Schematic distribution of the horizontal circulation is shown on (d): the Guinea Current (GC); the northern (nSEC), equatorial (eSEC), central (cSEC), southern South Equatorial Current (sSEC); the Equatorial Undercurrent (EUC); the Angola Current (AC); the South Equatorial Countercurrent (SECC) and Angola Benguela Frontal zone (ABF) (see Hopkins et al., 2013; Lass & Mohrholz, 2008; Talley et al., 2011). ISAS SSS are provided by the Coriolis center via the Copernicus website (http://www.coriolis.eu.org) (Gaillard et al., 2016). SMOS, Soil Moisture and Ocean Salinity; SSS, Sea Surface Salinity.

adequate for observing near coastal fresh water plumes (Boutin et al., 2018). The data set was obtained from the French Centre Aval de Traitement des Données SMOS (CATDS, https://www.catds.fr/).

This data set allows to well observe the SSS variability in the GG. As revealed in Figure 1, the variability of the low salinity waters in the eastern part of the GG determined from SMOS products is found significantly higher than the one inferred from objectively analyzed SSS fields built from in situ observations alone, the In Situ Analyses System—ISAS—products (Kolodziejczyk et al., 2017). SMOS SSS data enable to observe a clear low salinity signature in the region of the Congo River plume (Figures 1a and 1b). It also reveals, for
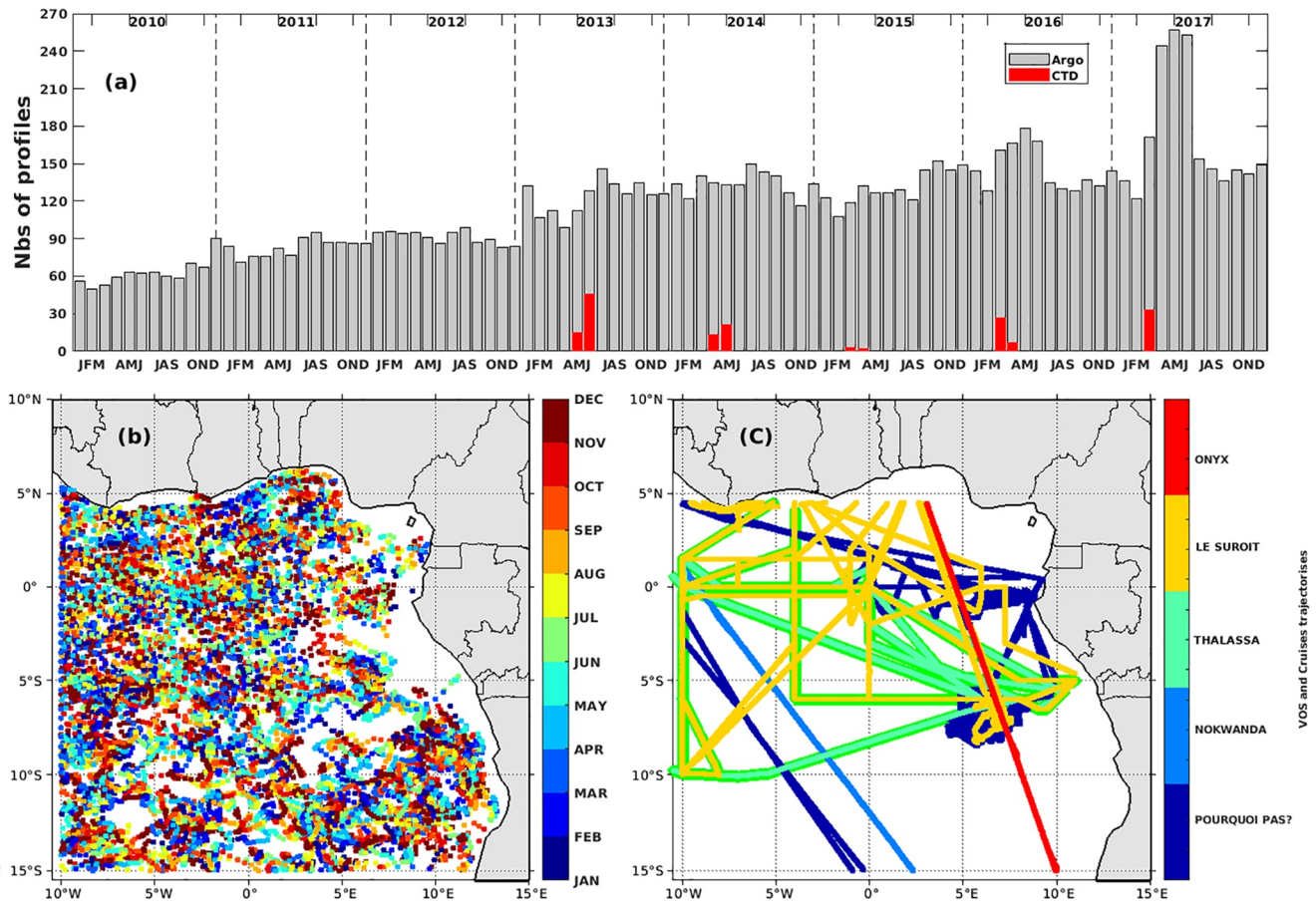
Figure 2. (a) History of Argo float and CTD PIRATA FR profiles from 2010 to 2017 in the Gulf of Guinea; (b) Spatial distribution of the profiles per month; (c) VOS (ONYX, NOKWANDA, and POURQUOI PAS?) trajectories for TSG SSS measurements and PIRATA (LE SUROIT and THALASSA) cruises in the GG. CTD, Conductivity Temperature Depth; GG, Gulf of Guinea; SSS, Sea Surface Salinity.

the first time, a strong and more realistic SSS seasonal amplitude (more than 2 pss in the eastern GG) within plumes area (Figures 1c and 1d).

For the purpose of the present study, we have also evaluated the accuracy and representativeness of SMOS SSS from in situ data available in the eastern GG, described in the following paragraph. In situ and satellite SSS data are in good agreement, with root mean square deviation (RMSD) of 0.4 pss and a high linear correlation coefficient of $r = 0.94$ at a 95% significance level (see Appendix A). As shown in the Amazon-Orinoco and in the Bay of Bengal plume regions (Akhil et al., 2016; Boutin et al., 2018; Fournier et al., 2015), SMOS SSS data exhibit a good signal-to-noise ratio and thus are reliable and accurate enough to address the seasonal variability of freshwater plumes in the GG and near the coast. Note that in the eastern GG, the SSS variability deduced from the SMOS SSS data is mostly dominated by the seasonal signal, while the interannual signal is significantly weak (not shown, see Figure S1).

2.2. In Situ Data

In situ salinity and temperature data are used to validate the SMOS SSS product (see Appendix A) and to provide subsurface hydrological observations needed to compute a salinity mixed layer budget. Thermosalinograph Sea Surface Salinity (TSG SSS) measurements are obtained from Voluntary Observing Ships—VOS—(Alory et al., 2015) and research vessels (Gaillard et al., 2015) (Figure 2c). These data have been quality controlled in delayed mode and calibrated by the French SNO-SSS (Service National d'Observation SSS; http://www.legos.obs-mip.fr/observations/sss/) and by researchers from the Laboratoire d'Océanographie Physique et Spatiale (LOPS, https://www.umr-lops.fr/). TSG SSS are available at 5-min time resolution

and are representative of salinity within the near-surface 10-m depth. They are yearly updated and freely available (Alory et al., 2015; Kolodziejczyk et al., 2020).

Temperature and Salinity (T/S) profiles from autonomous Argo floats are provided by the international Argo program since the early 2000s (Riser et al., 2016). For the purpose of this study, 13,030 individual T/S Argo profiles from 2010 to 2017 have been used. The selected profiles were downloaded from the Global Data Assembly Center for Argo (GDAC) (Argo, 2020). They are in delayed mode and individual data selected have a quality flag set to 1 (Figures 2a and 2b). Remaining suspicious profiles were rejected after control and visual check. For the MLD computation purpose, we only took into account the profiles for which: (1) the first depth of measurement is shallower than, or, equal to, 10-m depth and (2) T/S data that are available at least over a depth greater than 30 m, because MLD encountered in the eastern tropical Atlantic is generally shallower than this particular depth (de Boyer Montégut et al., 2004; Dossa et al., 2019). Based on these selection criteria, 11,304 Argo profiles were used.

Conductivity Temperature Depth (CTD) profiles were obtained during French yearly research cruises carried out from 2013 to 2017 in the framework of the PIRATA program (Bourlès et al., 2019). 166 PIRATA CTD casts have been carefully controlled and post-calibrated (Bourlès, Rousselot, et al., 2018).

2.3. Surface Freshwater Flux Data

In this study, we used the Objectively Analyzed air-sea Fluxes (OAFlux) evaporation data product, with $1° \times 1°$ horizontal resolution and monthly time step. Precipitation data were obtained from Tropical Rainfall Measurement Mission (TRMM 3B42; http://apdrc.soest.hawaii.edu/datadoc/trmm_3b42_daily.php), with 1/4° spatial resolution and daily time record. Both data sets cover the period from 2010 to 2017.

The GG is fed by more than 13 rivers (Mahé, 1991). Only Congo and Niger rivers (~81% of rivers discharge in the GG) are considered hereafter. The Congo River is the second strongest discharge in the world, with a runoff of 40×10^3 m³/s on average (Berger et al., 2014; Mahé & Olivry, 1999), while Niger River is ranked 24th, with 6×10^3 m³/s (Dai & Trenberth, 2002; Kang et al., 2013). Both runoff data were collected as continuous monthly time series over 2010–2017 from observatory service HYdro-geochemistry of the AMazonian Basin (SO-HYBAM, http://www.ore-hybam.org/index.php/eng/Data) and from NCAR (Dai, 2017) database for the period 2006–2014, respectively.

2.4. Surface Currents and Wind Data

The Geostrophic and Ekman Current Observatory (GEKCO) product provides an estimate of surface current on a 1/4° grid at global scale and is produced daily (Sudre et al., 2013). The Ocean Surface Current Analysis Realtime (OSCAR) currents, available with $0.33° \times 0.33° \times 5$ days grid resolution are also used. OSCAR product is currents averaged over the top 30-m (Lagerloef, 2002; Lagerloef et al., 1999), while GEKCO product represents the top 15-m depth dynamics (Sudre et al., 2013). Both GEKCO and OSCAR horizontal velocity are estimated from satellite altimetry and satellite wind stress products, thus including geostrophic and Ekman components (available over 2010–2017). In addition, we used the mean monthly climatology of near-surface velocity from satellite-tracked drifting buoy observations (the so-called DRIFTER currents) available on a $0.25° \times 0.25°$ grid resolution (Laurindo et al., 2017). We also used ANDRO surface current products that are estimated from Argo floats surface drifts. They provide an estimate of ocean circulation in the top 2-m depth (Ollitrault & Rannou, 2013). Finally, ADCP currents (150 kHz) from the French research cruise PIRATA FR 2017 (Bourlès, Herbert, et al., 2018) are used to highlight the vertical structure of ocean currents off Congo. They are provided with a 4-m vertical resolution and from a depth of 16 m. In addition, we used the wind data provided by the Global Ocean—Wind Analysis to characterize the wind regime over the GG, which are monthly averaged products with a 0.25×0.25 spatial resolution (Bentamy & Fillon, 2012).

3. Method

3.1. Freshwater Plume Pathway

The isohaline 34.5 pss has been chosen to track freshwater plume horizontal extension. This isohaline well characterizes the SSS front between the coastal area and the open ocean. It corresponds to SSS anomalies of −0.5 pss with respect to the monthly mean SSS value of 35 pss found in the GG (as determined from SMOS SSS). For the Congo River plume region, the ocean surface domain covered by SSS under this threshold value is found to be similar to the region where monthly SSS is anticorrelated with the observed monthly river discharge with a correlation coefficient of −0.5 (with 99% confidence level) or less, according to Chao et al. (2015).

3.2. Near Surface Salinity Budget Equation

To diagnose the physical processes driving the freshwater plumes variability in the GG, we performed a salinity budget within the upper ocean mixed layer. This approach has been widely used in the literature for investigating the processes of seasonal and interannual SSS variability within the ocean superficial layer in the Tropical Atlantic, from both observation data and numerical model outputs (e.g., Awo et al., 2018; Camara et al., 2015; Da-Allada et al., 2013; Kolodziejczyk & Gaillard, 2013; Vialard et al., 2001). Combining Moisan and Niiler (1998) and Köhler et al. (2018) approaches, the MLS evolution equation (Equation 1) can be written as follows:

$$\frac{\partial \overline{S}}{\partial t} = \underbrace{-\overline{u}.\nabla\overline{S}}_{ZADV} \underbrace{-\overline{v}.\nabla\overline{S}}_{MADV} + \underbrace{\frac{E-P-R}{h}SSS}_{SFFLUX} - \underbrace{\frac{1}{h}W_e.\left(\overline{S}-S_{-h}\right)}_{ENT} + \underbrace{\overline{k_H\nabla_H^2 S}}_{HDIFF} + R_e \tag{1}$$

with:

$$R_e = \underbrace{\frac{-1}{h}\left(k_Z\frac{\partial S}{\partial z}\right)_{z=-h}}_{VDIFF} - \underbrace{\frac{1}{h}\nabla.h\left(\hat{V}\hat{S}\right)}_{\text{Vertical shear}} - \underbrace{\overline{\nabla.V'S'}}_{EHADV} + \underbrace{\frac{1}{h}\left(w'S'\right)_{z=-h}}_{EVADV} \tag{2}$$

$$W_e = H_e\left(\frac{\partial h}{\partial t} + V_{-h}\cdot\nabla h + w_{-h}\right) \tag{3}$$

The depth-averaged of any variable over the MLD (h) is defined as: $\overline{a} = \left(1/h\right)\int_{-h}^{0} a\,dz$ and the deviation from this average is noted as $\hat{a} = a - \overline{a}$. $\nabla \equiv \left(\left(\partial/\partial x\right),\left(\partial/\partial y\right)\right)$ is the horizontal gradient operator (x and y are eastward and northward coordinates, respectively).

In Equation 1, S is the mean monthly MLS; V is the mean monthly horizontal velocity (including Ekman velocity and geostrophic velocity) with $\left(u,v\right)$ the zonal (x) and meridional (y) components of the velocity; E, evaporation, P, precipitation, and R, the River runoff. k_H is the horizontal diffusion coefficient, considered to be equal to 2,000 m^2 s^{-1} (Da-Allada et al., 2013) and k_Z is the vertical diffusion coefficient. S_{-h} characterizes the salinity at 10 m below the MLD (Berger et al., 2014).

From left to right, individual terms of Equation 1 are: The MLS S tendency, mean zonal (ZADV) and meridional (MADV) advection, surface freshwater flux (SFFLUX), entrainment at the base of the mixing layer (ENT), horizontal diffusion (HDIFF), and a residual (R_e). The residual term (Equation 2) includes the vertical diffusion (VDIFF), the vertical shear, the eddy horizontal (EHADV), and the vertical (EVADV) salinity advection processes. The residual term also includes the sum of all un-estimated physical terms and the accumulated errors from other terms. The eddy salinity advection terms are the temporal derivative from the mean salinity advection.

W_e *is* the entrainment velocity (Equation 3) at the base of the mixed layer. Only positive vertical velocities are considered and the detrainment (downward movement, negative velocities) is set to zero, since the water mass that flows out from the base of the mixed layer has the same properties as the water in the mixed layer, and does not affect the salinity in the MLS (Da-allada et al., 2013; Foltz et al., 2004; Ren & Riser, 2009; Ren et al., 2011; Schlundt et al., 2014). This constraint is setup with the use of the Heaviside step function: $H_e(x) = \{1, x \geq 0 \text{ and } 0, x < 0\}$ in Equation 1.

w_{-h} is the vertical velocity at base of the MLD, and is estimated from the continuity equation. Following Wade et al. (2011), we assumed that the horizontal divergence is depth independent in the mixed layer, so that the vertical velocity at the mixed layer base is expressed as:

$$w_{-h} = h\left[\frac{\partial u}{\partial x} + \frac{\partial v}{\partial y}\right]$$ (4)

Due to the constraints of the observation data available, we assumed that the surface horizontal velocities are representative of the velocities $V_{-h} = (u_{-h}, v_{-h})$ at the base of mixed layer.

According to Foltz et al. (2004), we assume that SSS is representative of the MLS (Da-Allada et al., 2013, 2014). Therefore, in the following, no distinction will be made between the MLS and the SSS. The MLD is computed with individual T/S profiles, by 0.03 kg m^{-3} density criterion relative to the density at 10-m depth (de Boyer Montégut et al., 2004); then we applied an objective mapping interpolation to get the mean monthly climatology. The partial derivative terms of Equation 1 have been calculated with central difference on the 1/4° grid resolution. Data set with low spatial resolution has been regridded onto SMOS SSS grid resolution. Due to the constraints of the observation data available, and for the sake of coherence of time-step differential, each term of Equation 1 was computed with climatological monthly mean of each variable. This method allows to evaluate at the same variance level, the seasonal variability held in each term of Equation 1.

The MLS budget is averaged in two boxes defined in Figure 1c. These boxes are chosen with three criteria, to investigate the physical processes behind the dynamics of the freshwater plumes in the eastern GG. The boxes encompass (i) the rivers' mouth, (ii) the highest variability of SSS (area covered by SSS seasonal cycle STD more than ~1 pss, Figure 1c), and (iii) the furthest offshore extension of low SSS pattern (the far-field region of freshwater plume) to encompass the full extension of freshwater plumes. The northern box is presently smaller, but its size does not matter. We have tested the size of the northern box for many dimensions and the seasonal cycle of the budget is still the same. Following these criteria, the diagnostic of salinity budget performed below is expected to reveal the physical processes that control the freshwater plume variability in the eastern GG.

4. Results

4.1. Horizontal Variability of Freshwater Plumes in the GG

The seasonal cycles of the monthly mean precipitation rate and runoffs off Congo and Niger rivers mouths are shown in Figure 3. In the Niger box, rainfall rates present a semi-annual cycle with maxima in May–June and October–November and minima in January and August, related to the back and forth meridional displacement of the ITCZ in the northern part of the GG (Diakhaté et al., 2016; Gu & Adler, 2004; Materi et al., 2012). The Niger River runoff exhibits an annual cycle with maximum runoff in September–October (Figure 3, top panel).

In contrast, the Congo River plume (Congo box) is weakly influenced by the ITCZ seasonal meridional migration (Materia et al., 2012). Consequently, the precipitation in the Congo region follows an annual cycle with a peak observed over November–April. The Congo River exhibits a large discharge throughout the year peaking from November to January. The Congo runoff dominates the freshwater flux and during October–January, the freshwater input is mainly dominated by the Congo River discharge which contributes by more than 78% with a maximum flux of ~61 × 10³ m³/s in the Congo box (Figure 3, bottom panel). In contrast, in the Niger box, the rain rate explains more than 89% of the freshwater fluxes (~40 × 10³ m³/s) during the maximum river discharge season (September–November) (Figure 3, upper panel).
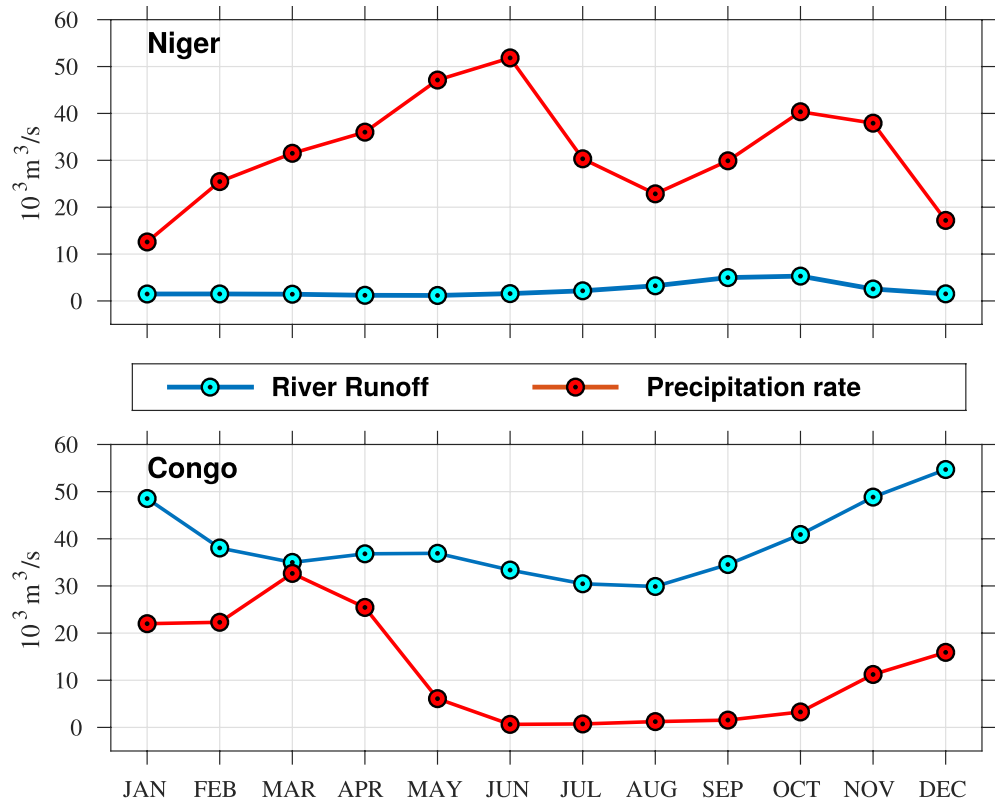
Figure 3. The 2010–2017 averaged seasonal cycle of precipitation rate (red curve; m³/s) and rivers runoff (blue curve; m³/s) integrated over the Niger box (top panel) and Congo box (bottom panel). The boxes are those defined in Figure 1c.

The 2010–2017 mean monthly climatology of SSS and surface currents in the GG are shown in Figure 4. Spatial and temporal variability of freshwater plumes distribution/extension are well detailed. The isohaline 34.5 pss is drawn to delimit the horizontal extension of the freshwater plumes. One can distinguish two regions of low SSS (hereafter named as freshwater plumes): (i) Niger region freshwater plume (including Niger River outflows) located in the northeastern GG (including Bight of Biafra and Bight of Benin) and (ii) Congo region freshwater plume (including Congo River outflows), in the southeastern GG.

From September to December, the freshwater plume off Congo extends northwestward along the coast until it connects to the Niger freshwater plume. During these months, the northernmost area of the eastern GG freshwater plumes is observed to extend progressively westward along the northern coasts of GG from 5°E to 10°W, where it is also fed by other secondary rivers (such as Cavally, Sassandra, Bandama, and Comoe rivers). From January to April, one observes the circulation from west to east of a salty water tongue along the northern coast of GG (from 10°W to 4°E) and the associated southward detachment of the freshwater plume toward the equator. This coastal detachment of freshwater plume, likely by salty advection, could be tied to the Guinea Current (GC) seasonal reversal (Boisvert, 1967; Djakouré et al., 2017), or related to coastal trapped eddies, which reach their maximum intensity in boreal summer in the north of the GG (Djakouré et al., 2014). During that period, the 34.5 isohaline surrounding the southern part of the Congo freshwater plume progressively extends southward along the Angola coast from 10°S in January to reach 12°S in March. The GG's north and south freshwater plumes then merge to form a wide freshwater plume reaching a maximum surface area extension around April. The surface currents distribution is mostly southeastward offshore of ~330–440-km width band along the coast, within low SSS patterns over this period.

From May to August, an abrupt surface salinization is observed along the equator off Cape Lopez (latitude 0°37′46″S), reaching up to 36 pss. In the equatorial band (±5° around the equator), this corresponds to an increase of about +0.7 pss with respect to the January–April period. This surface salinization splits the merged freshwater plume of the eastern GG into two distinct patches of low SSS patterns extending apart
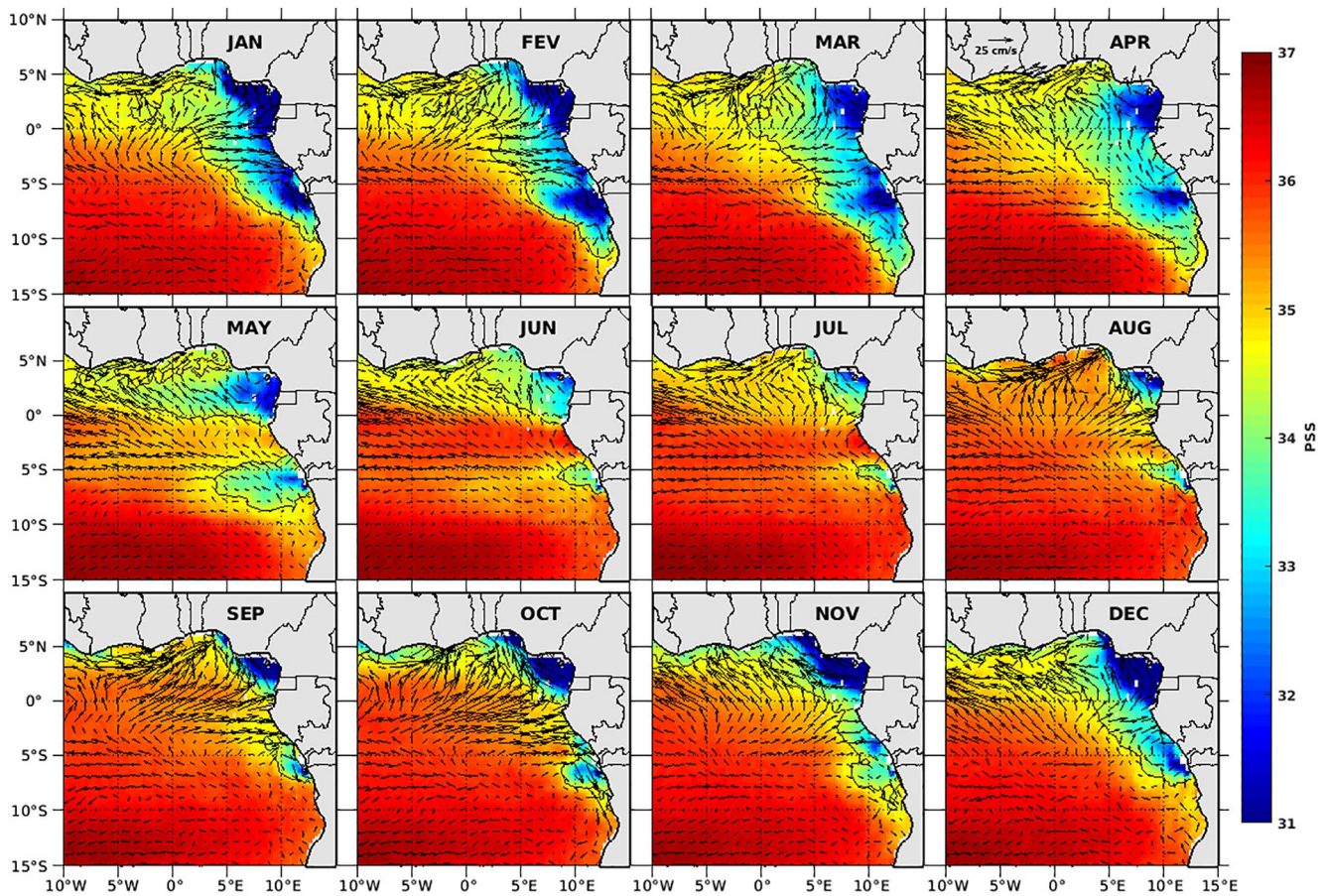
Figure 4. The 2010–2017 averaged monthly maps of SMOS SSS in the Gulf of Guinea. The black solid contours indicate the isohaline 34.5 pss, chosen to follow the freshwater surface spreading. The superimposed arrows (cm/s) represent the surface currents from GEKCO. SSS, Sea Surface Salinity.

of the equator. The zonal extension of the northeastern freshwater plume then significantly reduces during that part of the season with the 34.5 isohaline displaced along a central latitude of 3°N from 5°W in May to ∼5°E in August.

In May, the Congo region freshwater plume reaches a maximum westward extension until 4°E along 6°S, that is, the westernmost tip of the plume is located at a distance of about ∼950 km from the Congo River mouth. In June, the 34.5 isohaline is abruptly displaced eastward toward the Congo coasts up to 8°E, where the westernmost tip of Congo freshwater plume is observed almost stationary for the next two months (see summary movie in supporting information).

During boreal summer (over late June–September), the weak rivers runoff and relative minimum of precipitations reduce the freshwater input in the eastern GG (Figure 3). Therefore, this results in minimum freshwater plumes extension in the eastern GG in August. Clearly, the freshwater inputs in the eastern GG are consistent with the low SSS seasonal distribution (Figures 3 and 4). However, the freshwater plumes extension could not be explained by the horizontal advection only, since the low SSS patterns are not always coherent with the surface currents. For example, in February, part of the Congo freshwater plume is oriented northwestward while the surface currents off the river mouth, between 6°S and 8°S, are flowing dominantly southeastward.

The wind regime in the GG indicates the quasi-permanent presence of south-easterlies surface winds south of the equator all along the year (Figure 5). The Ekman-driven circulation deflects surface water masses to the left of the wind direction in the southern hemisphere. Hence, the westward extension of freshwater layer south of the equator (off Congo), observed over boreal winter-spring (December–May)
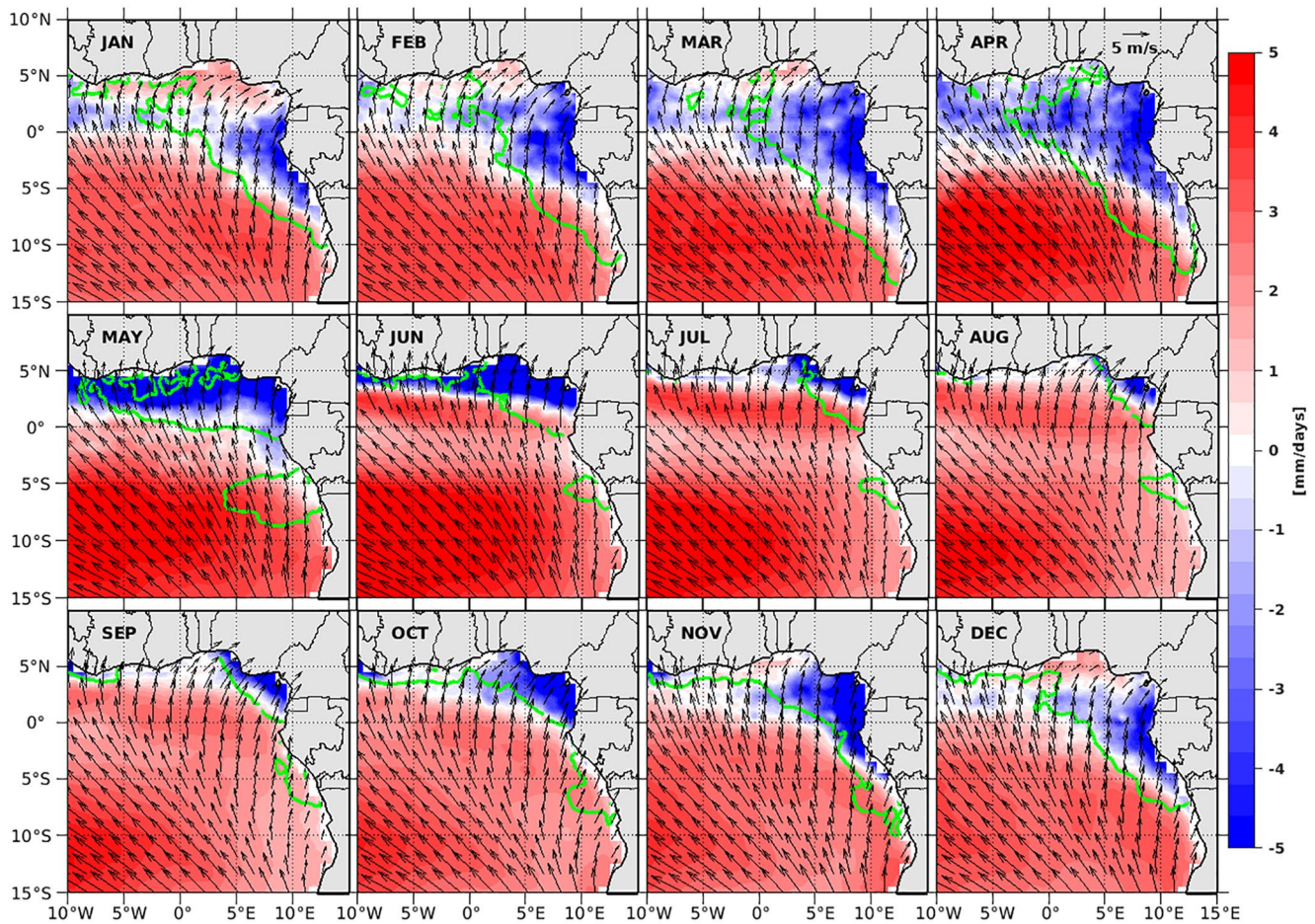
Figure 5. The 2010–2017 monthly mean maps of E-P (Evaporation minus Precipitation) balance in the GG (color shading). Green lines represent the isohaline 34.5 pss (delimitation of freshwater plumes areas from the coast to the open ocean; as shown in Figure 4). Arrows indicate the mean monthly climatological winds speed (m/s) at a 10-m level above the sea surface in the GG. GG, Gulf of Guinea.

could partly be explained by surface Ekman wind-driven currents. Contrarily, southwesterlies are prevalent almost all year long (but in May–June) in the northeastern most part of the GG, deflecting the surface waters eastward. Therefore, the wind-driven Ekman circulation cannot be responsible for the westward extension of the Niger region freshwater plume observed along the coasts of Nigeria to Liberia in September–November.

Qualitatively, there is a strong spatial correspondence between the seasonal variability of the precipitation and low SSS patterns throughout the seasons in the northern GG (Figures 4 and 5). There, during September–April, the low SSS and most intense rainfall patterns appear well correlated, contrarily to the Congo region freshwater plume, where the evaporation is predominant and the contribution of the precipitation on the SSS freshening is weak. Within the 0°S–5°S longitudinal band and from May to August, the E-P balance is largely dominated by evaporation, by about +3 mm/day. Evaporation therefore potentially reinforces the SSS increase of the freshwater plume signature in the equatorial band. Nevertheless, during May–November, south of 5°S, the evaporation excess over precipitation cannot explain the observed freshwater plume westward extension of the Congo region. Somehow, this is an indication that the impact of the atmospheric freshwater fluxes on the sea surface freshening is limited, and hence, brings out the contribution of other, ocean-related processes.
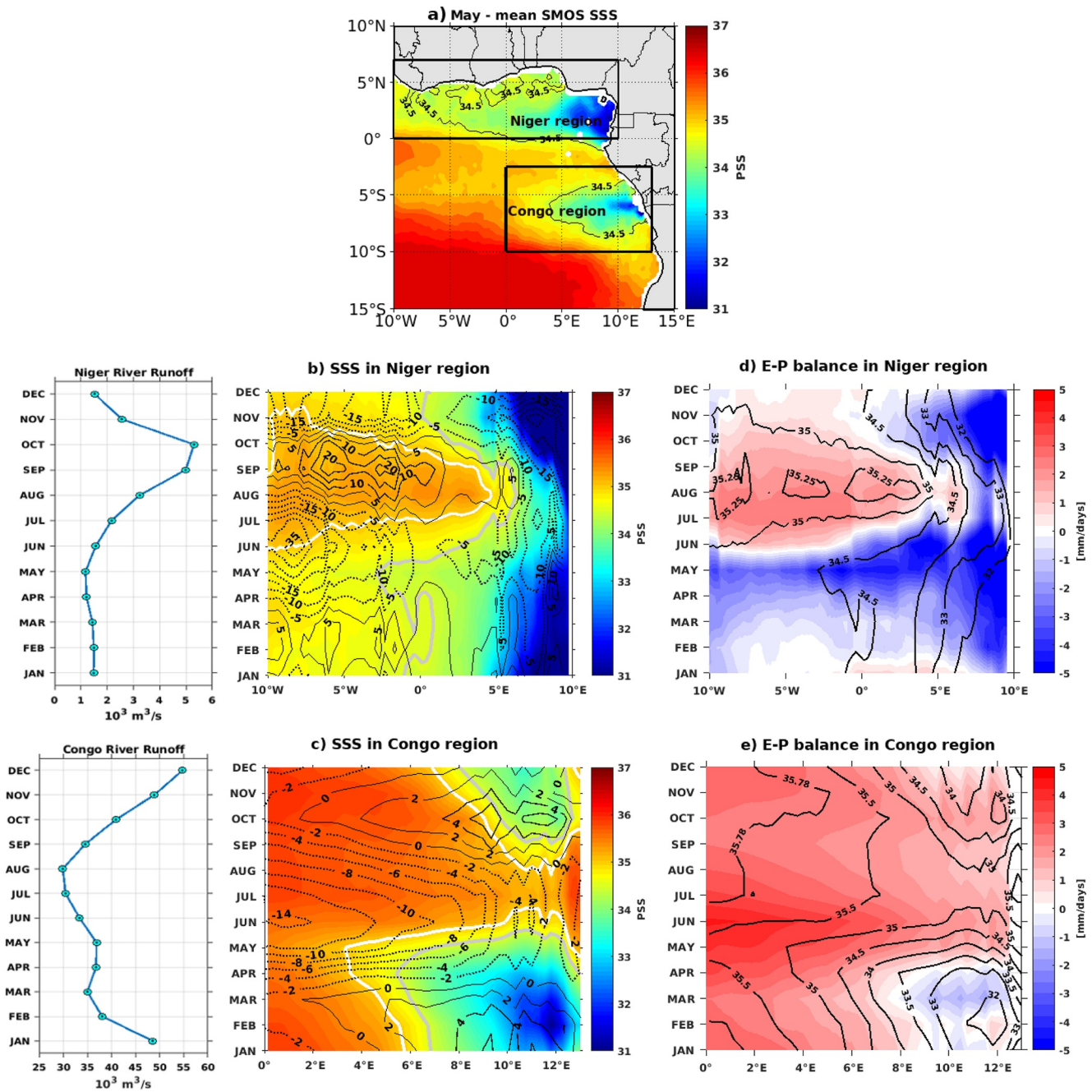
Figure 6. (a) SMOS SSS climatology for May with black thick rectangles showing the two spatial domains including GG's major freshwater plumes maximum westward extension. The thin black curve represents the 34.5 pss isohaline. (b) SSS time-longitude diagram in the northern box of the GG, that is, the Niger River plume region (0°N–6°N and 10°W–10°E); (c) SSS time-longitude diagram for the Congo River plume region (10°S–3°S and 0°E–13°E). Gray and white contours in (b) and (c) represent isohalines at 34.5 and 35 pss, respectively. The zonal currents amplitude derived from OSCAR product are given by black contours: solid and dashed lines show eastward and westward currents, respectively. Contour levels are given in unit of cm/s. (d) and (e) time-longitude diagrams of E-P flux (mm/day) in both Niger and Congo plume regions, where black contours correspond to SSS. The extreme left panel represents the rivers runoff seasonal cycle: Niger River (top left panel) and Congo River (bottom left panel). GG, Gulf of Guinea; SMOS, Soil Moisture and Ocean Salinity; SSS, Sea Surface Salinity.

4.2. SSS in Congo and Niger Freshwater Plumes Areas

To further documents the links between surface currents and the observed low SSS patterns seasonal distribution, longitude-time Hovmöller diagrams of the meridionally averaged SSS and surface currents are

shown in Figure 6 for the two boxes: the Niger freshwater plume region (0°N–6°N and 10°W–10°E) in the north of the GG and the Congo River plume region (10°S–3°S and 0°E–13°E) in the south. Note that these two boxes shown in Figure 6a are different from the ones shown in Figure 1c.

The surface waters in the Niger freshwater plume region are always fresher east of 5°E (mean SSS is less than 33 pss), than westward of this longitude (where the averaged SSS is greater than 34.5 pss), and a relatively saltier period is observed over the whole region between mid-May and September (Figure 6b). East of 5°E, the E-P balance is dominated by precipitation rate and exhibits nearly the same distribution as SSS (Figure 6d). In this region, one can also observe that the zonal currents are always westward. From September to April, the westward extension of low SSS appears consistent with westward zonal currents. In contrast, during May– August, no consistency can be seen between the observed saltier SSS pattern and zonal currents distribution.

Between 10°W and 5°E (Figure 6b), the westward current velocities keep increasing during April–May, due to the intensification of the northern branch of the SEC (Richardson & Reverdin, 1987). At the same time, relatively low SSS waters propagate westward with the 34.5 isohaline reaching its western most extension at ∼2°W in May, while a consistent pattern of high precipitation rate is observed. Then, from June onward, the SSS dramatically increases to reach a maximum (around 35 pss) in August, directly followed by a strong eastward current maximum (about 20 cm/s) in September. Evaporation is also found to be dominant over precipitation during that period (Figure 6d). The phase lag (about 2 months) between the setup of the SSS maximum and the eastward maximum velocities, suggests that zonal currents alone cannot explain the salinity changes during this period (Figure 6b).

In contrast, SSS seasonal cycle in the Congo freshwater plume region box reveals a period of low SSS which takes place from September to May in the eastern part of the box (east of 5°E), interspersed with a distinct high SSS event from June to mid-August (Figure 6c). The lowest SSS is observed from January to April (Figure 6c), with freshest values found around 10°E–12°E, following the Congo runoff maximum observed in December–January (Figure 3). At the same time, the E-P balance is dominated by precipitation, of ∼−2 mm/day (Figure 6e). From September to May, the westward low SSS extension occurs in two phases of the surface circulation: (i) During September–March, the westward freshwater propagation is opposite to the eastward flowing surface currents and (ii), during April–May, the low SSS area east of the 35 pss isohaline extends further westward concurrently with the intensification of westward zonal currents. Interestingly, from May to mid-September, between 6°E and 13°E, the sudden increase in SSS is observed with a concurrently westward intensification of the zonal currents.

Overall, the zonal distribution of the low SSS in the eastern GG appears to be partially influenced by the seasonal variability of the northern branch of the SEC and the GC. Yet, the zonal surface currents cannot explain the observed seasonal cycle of the fresh pools spatial distribution alone, especially in the Congo region and during the September–March freshwater westward extension. Quantitative analysis of both surface and subsurface processes is thus necessary to further understand the spreading and dispersal of these freshwater plumes. The physical processes controlling the near-surface salinity balance in the eastern GG are quantified in the next section.

4.3. Mixed Layer Salinity Budget

The far-field dynamics of freshwater plumes mostly depend on surface freshwater flux and related ocean dynamics through surface currents advection and vertical mixing processes (Horner-Devine et al., 2015; Katsura et al., 2015). To diagnose the physical mechanisms behind the freshwater plumes variations, an MLS budget has been calculated in the GG following Equation 1. Individual contributions from each physical process are presented. We focus on Niger and Congo freshwater plumes regions (the two boxes shown in Figure 1c).

4.3.1. Salinity Budget off Congo

Before considering the MLS budget, we first describe the MLS seasonal cycle averaged over the Congo box (Figure 7a). The MLS variation exhibits an annual cycle, with a salinity maximum in July. From mid-Au-
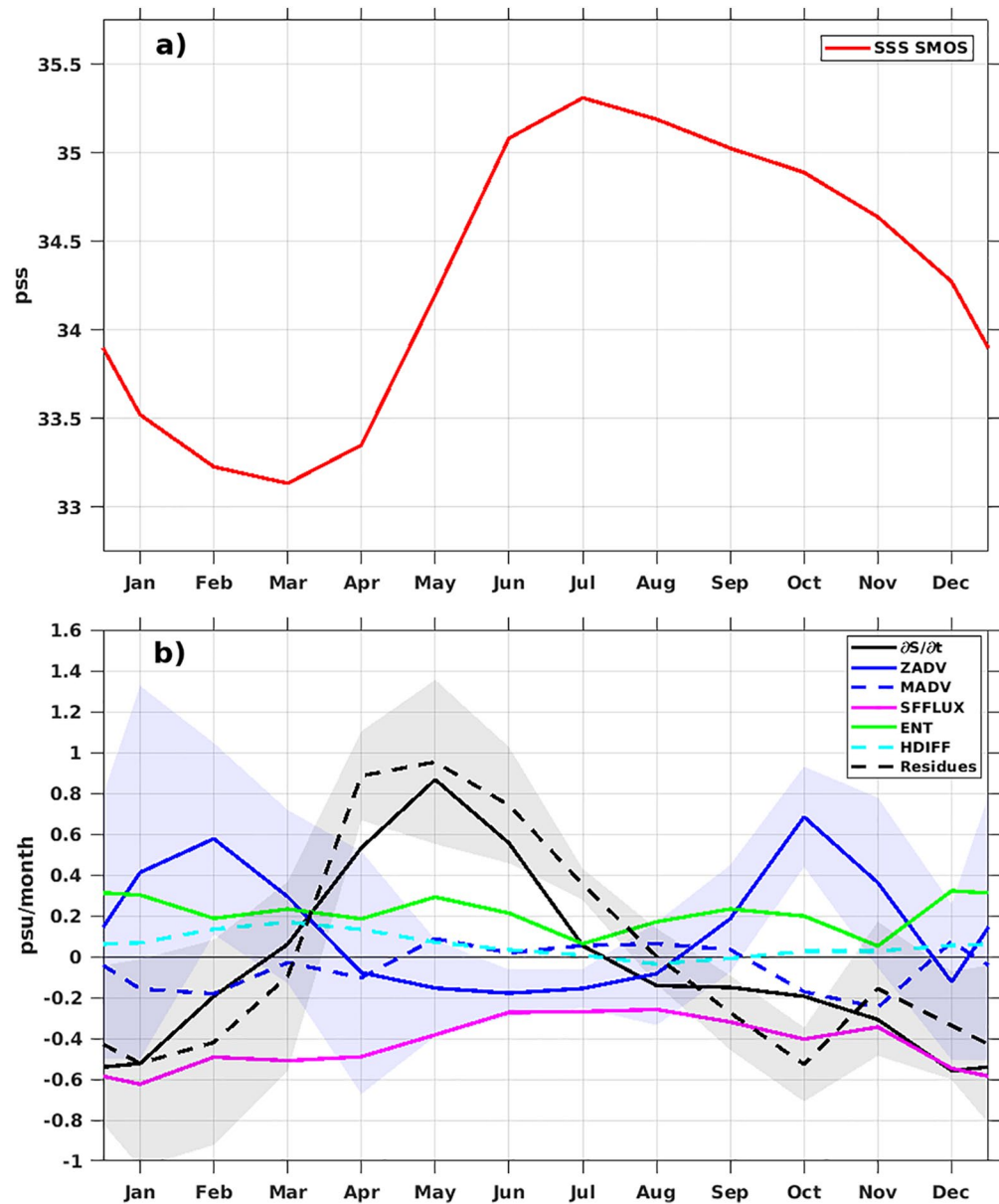
Figure 7. (a) Seasonal cycle of SSS averaged in the Congo box (see Figure 1c), from SMOS SSS (red curve); (b) Seasonal cycle of each term of near-surface salinity (MLS) budget in the Congo River plume: individual contributions to salinity tendency (solid black) of: Freshwater flux (purple), Entrainment (green), Horizontal diffusion (dashed cyan), Zonal advection (solid blue), Meridional advection (dashed blue), and Residues (dashed black). Terms are plotted with their sign according to the right side of Equation 1. The colored bands represent the standard deviations for zonal advection (light blue) and residue term (gray) associated with the spread of DRIFTER, OSCAR, GEKCO, and ANDRO surface currents computation. *Note.* All diagnostic terms are estimated by using the OSCAR current product. MLS, mixed layer salinity; SMOS, Soil Moisture and Ocean Salinity; SSS, Sea Surface Salinity.

gust to March, the MLS decreases progressively by ∼2 pss, reflecting the high Congo River discharge and precipitations during this period (Figure 3, bottom panel). During April–July, the MLS suddenly increases by ∼2 pss. The mechanisms driving the MLS cycle are discussed below.

The seasonal cycle of the individual contribution of each term in Equation 1 to MLS changes is presented in Figure 7b for the Congo freshwater plume region. In agreement with the freshening periods reported in previous sections (Figure 3), the salinity tendency presents a strong annual cycle. Two distinct periods of

variability can be reported: a negative salinity tendency period (NSTP) during mid-July to March, and a positive salinity tendency period (PSTP) over April–July. The maximum salinity tendency of 0.87 pss/month peak in May reflects the abrupt salinization observed during this period along and south of the equator and in the eastern GG. Continuous negative contribution of SFFLUX is observed all year round (about −0.4 pss/month on average). This freshening effect, enhanced by the intense Congo River runoff, is larger during NSTP (about −0.6 pss/month) when the ZADV is the largest driver of the MLS trends together with the SFFLUX. The salinity advection contribution increases surface salinity and peaks two times, in February and in October, with a rate of ∼0.6 pss/month. During NSTP, the zonal eastward currents (Figure 6c) advect the offshore salty water toward the Congo area characterized by buoyant freshwater flux anomalies, which could be a potential source of vertical mixing in the water column. As compensation effect, the MADV is negative, more or less of −0.2 pss/month, whereas the residual term acts as opposite signal to the ZADV, by fitting more or less the salinity trends. The HDIFF off Congo is small all year round, except during the transition between NSTP and PSTP around March, where it rises to ∼0.2 pss/month.

During PSTP, the residual term well fits the salinity trends cycle. It is remarkably the major driver of salinity changes, pointing out the potential contribution of subsurface processes through VDIFF. The ZADV is weak and nearly constant (−0.2 pss/month on average), whereas the MADV effects are almost negligible during PSTP. This suggests that the high surface salinization observed in May, associated with the dissipation of the low SSS patterns observed until August (Figures 4 and 6c), is related to subsurface processes. The entrainment at the base of the MLD also contributes to increase the MLS. It peaks in May, supplying salty water across the mixed layer base that enhances the surface salinization (Figures 6c and 7a). The dominance of the residual terms during this period suggests that vertical processes may explain the increase of salinity in the region.

4.3.2. Salinity Budget in Niger River Plume Region

Like in the Congo box, the MLS exhibits an annual cycle in the Niger box (Figure 8a). From December to August, the MLS increases progressively by ∼+3 pss, then abruptly decreases the rest of the year. The amplitude of the MLS seasonal cycle in the Niger box is strong, about ∼3.5 pss, with lower minimum salinity (of ∼31 pss) than that observed in the Congo freshwater plume region (∼33 pss). Such differences between Niger and Congo boxes MLS cycles cannot be explained by rivers runoffs and precipitation only, and suggest that these two regions are subjected to different oceanic processes that interact differently on the freshwater fluxes.

The seasonal cycle of the salinity tendency and individual contributions within the Niger box is shown in Figure 8b. From December to mid-July, a positive and nearly constant salinity tendency of ∼+0.5 pss/month is observed. All diagnostic terms almost inter-compensate each other, but are strongly dominated by entrainment and horizontal advection (both ZADV and MADV). The entrainment term and the residues (negative contribution) nevertheless exhibit opposite peaks in February. The NSTP is observed from August to November in this region, with maximum peak of salinity decrease of $\left(\partial \overline{S} / \partial t \right) \sim −1.2$ pss/month. ZADV appears to be the dominant driver of the MLS variation during that period. It reaches a maximum of ∼−4.6 pss/month, whilst MADV, entrainment and the residual term exhibit a positive compensating contribution. The weakening of the GC during boreal fall-winter (Lemasson & Rebert, 1973) gives rise to an intense (of ∼−15 cm/s) westward reversal current (Figure 6b) and could explain the intense westward advection of low SSS along the northern coasts of the GG. One can notice the weak variations of the SFFLUX (dominated by precipitation and Niger River runoff) all year round if compared to dynamical contributions.

4.3.3. Sensitivity to the Surface Currents Products

To better understand the large residual terms found in the MLS budget analysis, a sensitivity analysis has been performed on advection and residual terms by using various current products (Drifters, GEKCO, OSCAR or ANDRO surface velocities, Figures 9a and 9b), then separating geostrophic and Ekman current components. The horizontal advection terms computed from various products and residuals present the largest differences during the periods of low SSS, when precipitation and rivers runoffs are the highest: September–March off Congo and September–November in the Niger freshwater plume region (Figures 9a–9d). Residual terms appear mostly negative during the period of development of freshwater plumes, associated with low SSS (Figures 9c and 9d). This negative residual is difficult to interpret in terms of vertical water
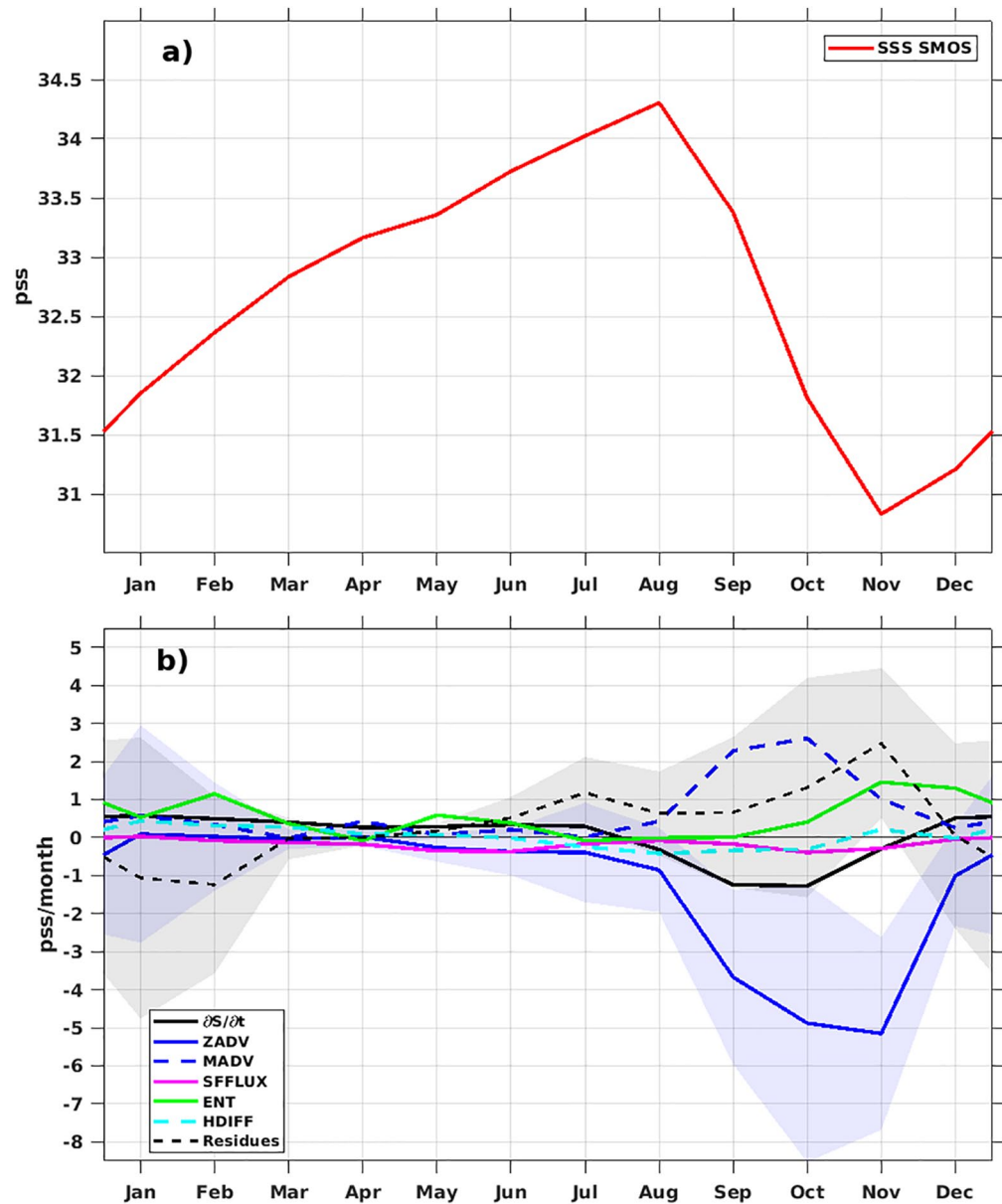
Figure 8. Same as in Figure 7 but for the Niger freshwater plume region—northeastern most part of GG (Niger box, Figure 1c). *Note*. There is a scale difference between *Y*–axis in Figures 7 and 8. GG, Gulf of Guinea.

flux in the region of freshwater plumes: vertical water mass flux cannot decrease salinity since saltier water is underlying the freshwater plume. In addition, the disparity and non-convergence of the residual terms observed in the Niger box (Figure 9c, from September onward), seem complex to explain. The standard deviations of advection and residual terms computed from the four products increase during the periods of low SSS (Figures 9g and 9h). This suggests large uncertainties among the surface currents products to properly represent the advection within freshwater plumes during these periods. Uncertainties associated with each term in Equation 1 also showed that horizontal advection (both zonal and meridional, from OSCAR product) estimations are related to the greatest uncertainties (see Appendix B for more detail). However, it is worth noticing, that the negative contribution of residuals is reduced to nearly zero in the Congo box when using Ekman currents alone (from GEKCO product) (Figure 9d). This suggests that, the dynamic of the freshwater plume extension during the low SSS period in the Congo box is likely explained by the Ekman component of advection process, indicating the primary influence of the shallow wind-driven current on
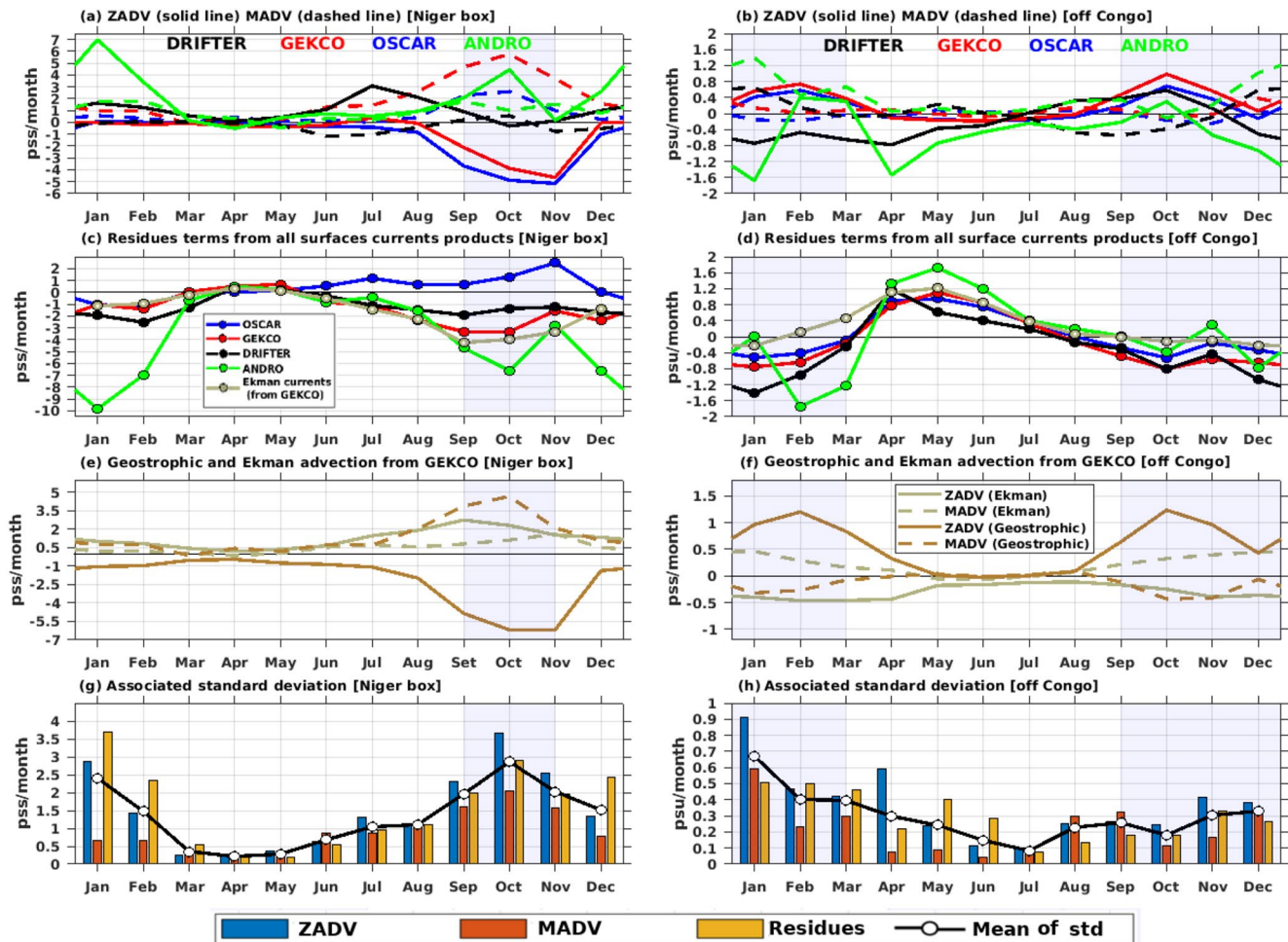
Figure 9. Diagnostic of SSS: (a, b) Zonal and Meridional advection; (c, d) Residues; and (e, f) contribution of Geostrophic and Ekman currents advection from GEKCO currents in Congo (right panels, Congo box) and Niger (left panels, Niger box) rivers plumes area from DRIFTER, GEKCO, OSCAR and ANDRO currents. (g, h) Associated standard deviation of zonal and Meridional advection, and Residues, computed from DRIFTER, GEKCO, OSCAR, and ANDRO products. *Note*. OSCAR currents product is mainly used for the salinity budget (presented in previous sections) because of the low amplitude (close to zero) found for the negative values of residual term, both in the Niger and Congo boxes. The vertical light-blue shaded patches correspond to the period of low SSS over which the largest differences are observed between the residuals terms and horizontal advection terms computed from various products: September–March off Congo and September-November in the Niger freshwater plume region. SSS, Sea Surface Salinity.

the Congo freshwater plume. In the Niger box, the residual term has remained almost unchanged with the same diagnosis by using only Ekman currents (Figure 9c).

An analysis of geostrophic and Ekman currents, made from the GEKCO currents product, shows that the estimated surface currents are predominantly geostrophic. The contribution of the Ekman advection is fairly weak compared to the geostrophic advection (Figures 9e and 9f). Angular deviations between satellite currents products (OSCAR and GEKCO) and in situ products (Drifter and ANDRO) are also observed (not shown, see Figures S2 and S6). They show weaker differences between the satellite OSCAR and GEKCO currents products than between Drifters and ANDRO ones. This difference could be related to the low sampling rate of the Drifter and ANDRO data in the eastern GG. Also, in presence of a strong vertical stratification, that the different products are representative of the currents at different depths (i.e., 30 m for OSCAR, 15 m for GEKCO and Drifter, and 2 m for ANDRO) could explain a large part of these differences. For example, at short time scale (over ~2 days) and between 8.5°E and 10°E off Congo (Figure 10), the northwestward spreading of the very shallow freshwater patterns (of ~15-m depth) is well shown in the S-ADCP currents measurements. More precisely, the vertical shear structure within the ocean surface layer
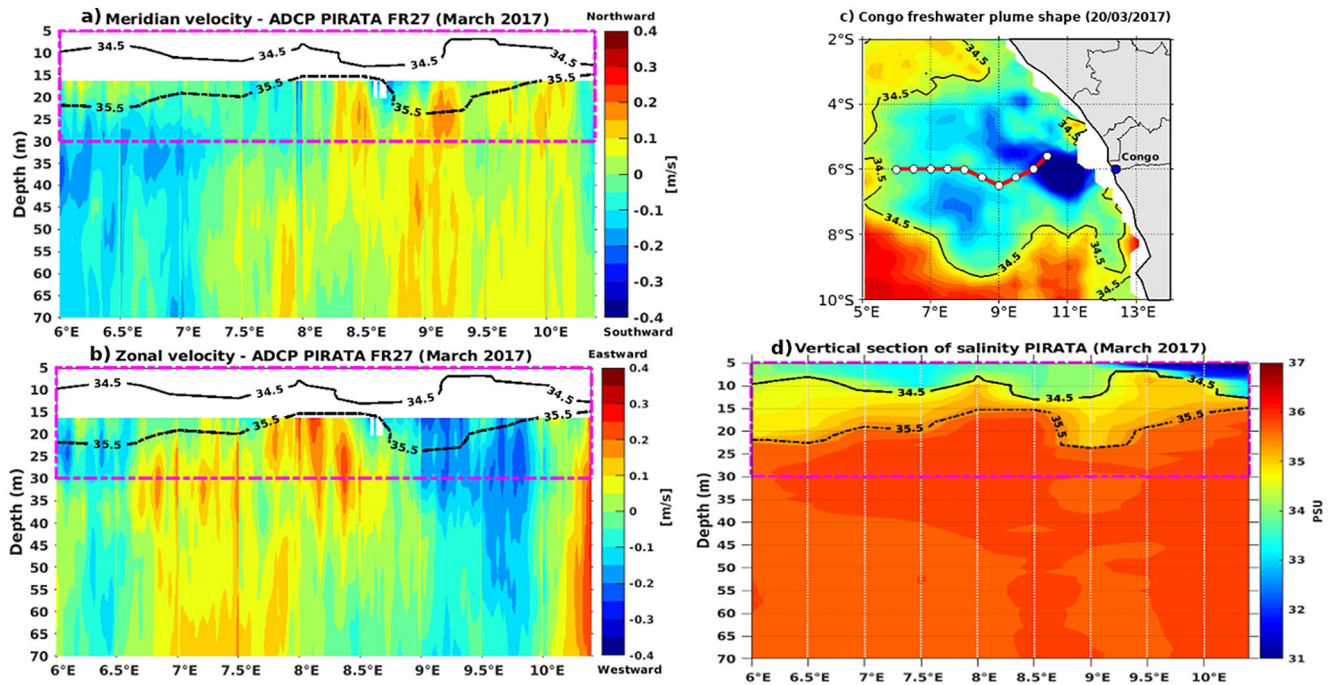
Figure 10. Zonal section of (a) meridional and (b) zonal S-ADCP currents velocities from PIRATA FR27 cruise (March 2017) off Congo. (c) Map of SSS on March 20, 2017 along with the transect of ADCP currents measurement (red line). (d) Zonal section of salinity off Congo from PIRATA FR27. The white points in (c) and the vertical white dashed lines in (d) represent the positions of CTD profiles. The black contours represent the isohaline 34.5 pss. The representative depth of 30 m for the OSCAR and GEKCO currents is indicated (dashed magenta boxes). CTD, Conductivity Temperature Depth; SSS, Sea Surface Salinity.

(∼0–30 m) shown in S-ADCP current measurements (Figures 10a and 10c) appears to be smoothed in the used GEKCO and OSCAR surface currents products. This suggests that the shallow Ekman-driven dynamic of freshwater plume may be not well represented, because of the predominance of geostrophic currents in GEKCO products (and likely in OSCAR) in the eastern GG (Figures 9e and 9f). By construction, altimeter-derived currents (OSCAR and GEKCO) can be misrepresentative of the shallowest currents potentially impacting the surface freshwater plume dynamics and other potential physical processes affecting the SSS. This sensitive analysis suggests that, in addition to the improved SSS data now available from SMOS, more realistic and representative currents data are needed for the very top layer to better describe and understand the dynamics of the thin freshwater plume.

5. Discussion and Conclusion

Long SSS time series available from SMOS satellite mission enabled an improved characterization of the spatiotemporal variability of the freshwater plumes in the GG. This study highlighted, for the first time, an unprecedented monitoring of the seasonal variability of the freshwater plumes in the eastern GG, particularly for the Congo River plume dynamics.

The eastern GG freshwater plumes seasonal evolution is characterized by two spreading regimes: northwestward along the coasts from late boreal fall to early winter (September–January) and southwestward redirection of the plumes from January until April, when their maximum offshore extend is recorded. This freshwater plumes evolution is mostly the result of the seasonal cycle of freshwater flux and ocean-related processes. In the northeastern most part of the GG, freshwater flux is dominated by both precipitation and runoffs, whilst in the southeast, it is mainly dominated by the Congo River runoff. The dissipation of freshwater plume patterns is handled by salty water upwelling along and south of the equator, which intensifies over late boreal spring until summer (May–August), with a minimum horizontal spread of the freshwater observed in August.

The dynamics of Congo and Niger freshwater plumes pathways fit as well the schematic shape of far-field dynamics of freshwater plumes systems inventoried by Horner-Devine et al. (2015). The initial far-field dynamic of these plumes (also strongly under the influence of the Earth's rotation) is a rightward deviation from the mouth of rivers, following the coastal geo-morphology, inducing (i) a northwestward propagation of the Congo freshwater plume (such as Eel River plume system; Geyer et al., 2000) and (ii) a westward propagation of the Niger freshwater plume (such as Mekong Delta plume system; Thanh et al., 2020) (see Figure 4, September–December). However, the freshwater plume far-field southwestward deviation (second regime of plumes spreading) observed in the eastern GG, is out of the classification of river plumes system by Horner-Devnie et al. (2015). This southward recirculation of freshwater plumes is forced by the near-coastal ocean surface currents (see Figure 4, January–March) and related large-scale ocean dynamical processes, such as surface currents advection (as discussed below).

Our findings are in agreement with previous studies that found isohalines less than 35 pss, nearly parallel to the coast and mostly northwestward in late boreal fall—October to November—in the eastern GG (Berrit & Donguy, 1964; Wauthy, 1977). Southward freshwater excursion observed from January to April (until 12°S, Figure 4) can be explained by the dynamic of the poleward coastal Angola Current and the northern branch of the cyclonic Angola Gyre (Figure 1d) associated with the South Equatorial Counter Current (Doi et al., 2007; Kopte, 2016; Scannell & McPhaden, 2018). These surface currents can advect the fresh and less dense Congo River water toward the south. One potential explanation for the westward excursion of the Congo River plume, is that the mean monthly wind directions over this period are nearly northward (Figure 5) and thus favorable for a westward wind-driven Ekman surface transport (see also Figures S3 and S4). As suggested by Reul, Quilfen, et al. (2014), southwestward plume extension depends on the prevailing wind stress in the Angola Basin. This is in agreement with Hopkins et al. (2013) who found that changes in the magnitude and direction of the wind stress and therefore the wind-induced currents are one of the main driving forces behind the variability of the Congo region freshwater plume. That also agrees with results by Vic et al. (2014) from a numerical model analysis (also by Chao, 1988), which shows that the Congo region freshwater plume is transported northwestward under the influence of the wind-driven surface Ekman currents. The authors also highlight that Congo freshwater plume is more likely surface trapped and that the amount of freshwater would be mostly contained in the offshore bulge rather than in the narrow coastal current. This freshwater pool can be advected far from the coast, up to 4°E.

Off Congo, the diagnostic of MLS budget reveals that, from late fall until boreal winter (NSTP), salinity changes are due to the SFFLUX prevalence and the nearly counterbalanced effects by ZADV and residual terms (see also supporting information Figure S5). The negative residues suggest a prevalence of eddies salinity advection over the vertical diffusion. However, the strong residues prevent precise determination of associated physical processes during this period.

Over the rest of the year (PSTP, from late spring to boreal summer—April–July), the SSS increase is due to the decreasing of SFFLUX combined with a peak of entrainment at the base of the mixed layer. Vertical mixing and eddies salinity advection (EHADV and EVADV), which are included in the residual term, increase significantly. This suggests that the SSS increase results from vertical mixing through diffusion and eddies processes (and related vertical shear). Prevalence of vertical processes and the northward wind present during this period (Figure 5), are favorable for salty water outcropping/upwelling, through offshore surface Ekman transport, so leading to freshwater plumes dissipation (by intensified mixing process). The SSS maximum events, induced by outcropping, are in agreement with previous studies based on numerical modeling by Kolodziejczyk et al. (2014). These authors found that the salty upper thermocline layer (a part of EUC core) outcrops along and south of the equator, and retroflects westward over this season. These maximum SSS values are observed when intense vertical shear and mixing processes are recorded (Da-Allada et al., 2017). Indeed, the increased horizontal shear between the EUC and the westward flowing SEC may intensify vertical mixing within the superficial layer (Da-Allada et al., 2017), thus increasing the salinity of the surface layers. This period corresponds to the peak season of the Atlantic Cold Tongue characterized by the presence of cold and salty water in the GG (Brandt et al., 2011; Da-Allada et al., 2017; Schlundt et al., 2014).

Furthermore, during late boreal summer until early winter in the northeastern most part of GG, the MLS changes within the freshwater plume are driven by counterbalanced effects of the horizontal advection

(both ZADV and MADV), the entrainment at the base of the mixed layer, and the residues. The maximum offshore Ekman transport that is present during boreal summer-fall (Bakun, 1978) could be supportive of the observed strong ZADV. That agrees with results by Da-Allada et al. (2014), who found that the seasonal cycle of near-surface salinity in the northeastern GG, is dominated by vertical diffusion, freshwater flux, and advection processes.

However, the seasonal cycle of diagnostic terms of the near-surface salinity budget presented here is not fully consistent with that found by Da-Allada et al. (2013). In the northeastern GG, these authors found a strong contribution of entrainment (up to ∼0.6 pss/month, their Figure 13h) during boreal spring, while our estimated entrainment appears by late fall until winter (about ∼1.5 pss/month, Figure 8b). Da-Allada et al. (2013) also showed that ZADV and entrainment are major drivers to explain the cycle of the SSS changes off Congo, while our findings indicate a strong contribution of SFFLUX and VDIFF together with ZADV. Differences could be related to the low resolution of SSS data sets and limited in situ data used by Da-Allada et al. (2013) (e.g., their Figure 1) to constrain their model. That the boxes used by these authors differ from the ones used in our study could also be one of the explanations. Furthermore, our findings agree with the results by Berger et al. (2014) who found that, in the Congo River plume region, salinity trends are mainly controlled by horizontal advection and subsurface processes (dominated with vertical mixing) (see also Da-Allada et al., 2014). However, they found that the SFFLUX forcing is weak (less than ∼−0.2 pss/month) compared to the dynamic contributions, while our diagnostics indicate that the SFFLUX contribution (up to ∼−0.6 pss/month) is important to explain salinity trends.

Uncertainties in the MLD estimation, the assumption of a constant horizontal diffusion coefficient (k_h), and that the runoff contributions from other rivers in the region (such as Ogooé, Sanaga) have been discarded certainly impact the closure of MLS budget, so contributing to the large amplitude of the residual term. These caveats might be particularly important for the MLS budget within the freshwater plumes, where vertical and horizontal mixing processes might be not properly represented. It is difficult to explicitly estimate the vertical processes (diffusion and shear) from the set of data at hand. It also appears tricky to explicitly close the MLS budget, because of likely misrepresented of very surface currents products in the eastern GG. The used in situ surface currents products (Drifter/ANDRO) integrate sparse data in the eastern GG. The satellite surface currents (OSACAR/GEKCO) are found to be mostly geostrophic, while the thin surface freshwater plumes in the GG seem to be influenced by the shallow Ekman surface transport. New challenges based on Satellite-borne Doppler Waves and Currents Scatterometers (Marié et al., 2020) measuring the very near-surface currents will be really supportive for future progress for freshwater plumes dynamics understanding.

Appendix A: SMOS SSS Validation From In Situ Measurements

The in situ measurements presented in Figure 2 are used as a reference data set to validate SMOS SSS in the GG. The in situ SSS measurements and SMOS SSS are collocated in time and space. The initial TSG SSS (with 5 min time step record) are reconstructed/smoothed to daily samples using a median filter within 0.25° × 0.25° grid cell, to better fit the SMOS SSS product resolution and to reduce as much as possible the representativeness error resulting from sampling differences between in situ and SMOS data.

The scatter plots between SMOS SSS and available in situ SSS measurements (from TSG, Argo, and CTD) in the GG are presented in Figure A1. In situ and satellite SSS are in good agreement, especially for salinity between 32 and 37 pss, with RMSD of 0.4 pss and a high correlation $r = 0.94$ at a 95% significance level. The linear regression line (green line) is almost merged with the identity function (black line), with an extremely small angular deviation of 1.45° and 3.14°, in case of Argo/CTD (Figure A1b) and TSG (Figure A1a) data, respectively. In the whole study area, SMOS SSS values are on average about 0.04 pss fresher than in situ measurements (Figure A1c). This systematic difference increases to ∼−0.13 pss on average (Table A1) for grid nodes located within a band of 150-km from the nearest coasts and is mainly associated with SSS lower than 32 pss. This fresh bias can be induced either by remaining residual landmass contamination in SMOS data, or by strong vertical salinity gradients often reported in river plumes (SMOS SSS is representative of the first centimeters below the surface, Boutin et al., 2016). Over the maximum extent area of freshwater plume, at least 800 km far from the coast, the systematic difference is about ∼−0.06 pss. The observed biases
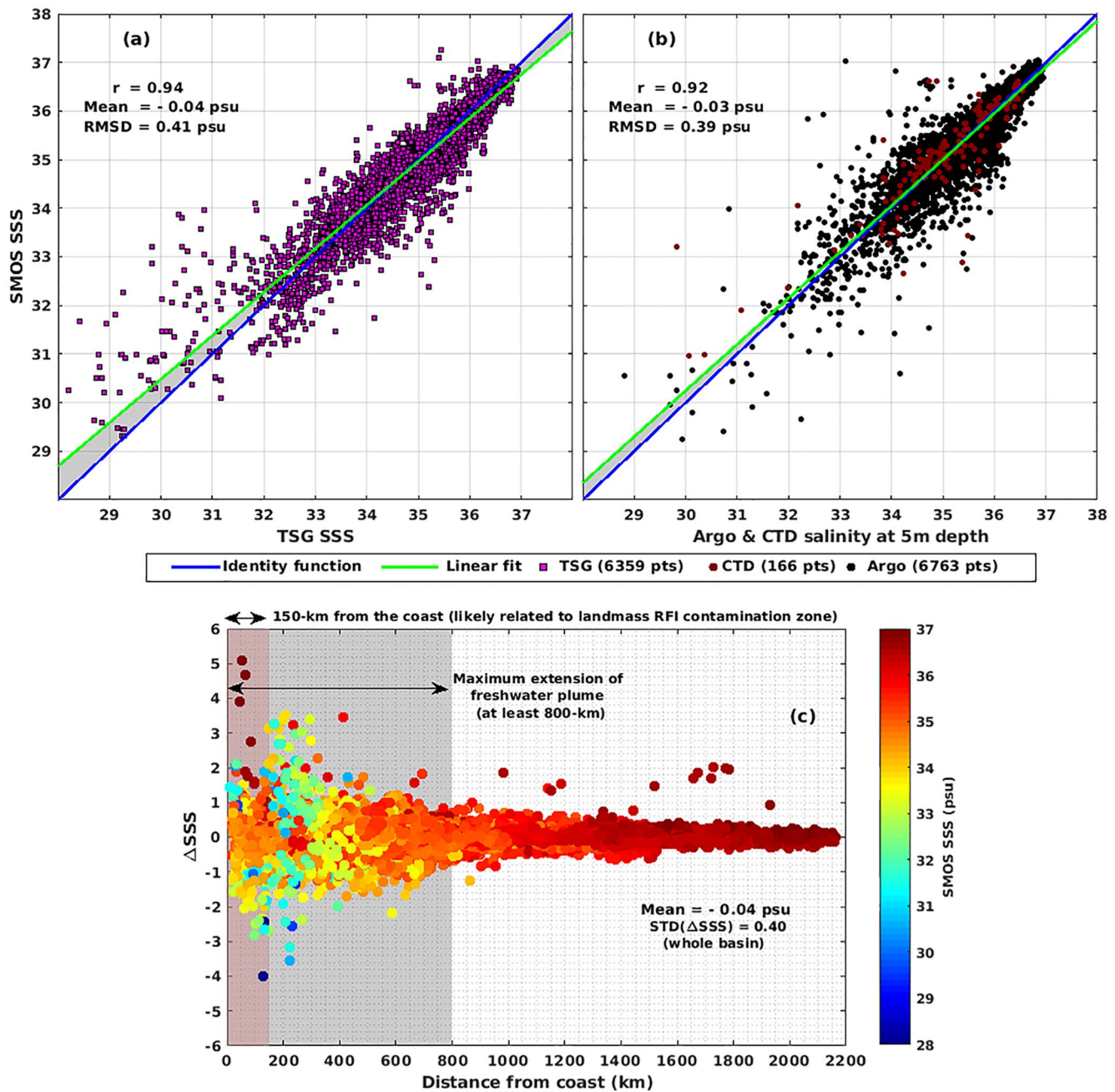
Figure A1. Scatter diagrams between SMOS and in situ SSS measurements: TSG SSS (a) and Argo & CTD salinity at 5-m depth (b) from 2010 to 2017 in the Gulf of Guinea; Figure (c) represents the SMOS SSS bias referred to in situ data, $\Delta SSS = SSS_{SMOS} - SSS_{in\ situ}$ as function of distance from the coast (colored dots). The color bar displays the associated SMOS SSS measurement. The likely landmass RFI contamination zone is shown with light red band and the maximum extension of freshwater plumes from the coast, in the light gray color band (at least 800 km from the coast to open ocean). The isobath 10 m is used as coastline for distance calculation. The mean value displayed on (a) and (b) are the averages of ΔSSS. CTD, Conductivity Temperature Depth; SMOS, Soil Moisture and Ocean Salinity; SSS, Sea Surface Salinity.

between the satellite and in situ SSS and the ΔSSS's STandard Deviation (STD) of 0.40 (Figure A1c) are relatively small compared to the range of seasonal STD of SMOS SSS—greater than 2 pss—in the eastern part of the GG (Figure 1c).

Despite the overall agreement, SMOS SSS data display large differences with in situ data up to ±3.5 pss for a couple of collocated points (mostly within a 200-km wide band from the coasts, Figure A1c). In the eastern

Table A1
The Mean Systematic Bias (ΔSSS) of SMOS SSS

Distance from the coast to offshore	150 km	800 km	Whole basin (~2,200 km)
Mean bias (ΔSSS)	−0.13 pss	−0.06 pss	−0.04 pss
	SMOS is on average fresher than in situ data		
STD (ΔSSS)	0.71	0.48	0.40
RMSD	0.72 pss	0.49 pss	0.40 pss
Correlation coefficient	0.86	0.90	0.94

Note. Related to in situ collocated data, biases standard deviation; the RMSD and the correlation coefficient as function of distance from the coast to offshore. each value given below represents the average in the area of the coast up to the distance indicated.

RMSD, root mean square deviation; SMOS, Soil Moisture and Ocean Salinity; SSS, Sea Surface Salinity.

GG freshwater plumes, this difference could be explained by the strong salinity stratification within the few meters depth at the top of the superficial layer (Akhil et al., 2016; Boutin et al., 2016, 2018; Fournier et al., 2017). Indeed, the radiometer estimates salinity within a few centimeters from the sea surface while the in situ data are point-wise measurements acquired around 5- to 10-m depth for VOS TSGs, and 5 m for CTD and Argo. The near-surface mixing conditions can also explain some of the observed differences. In low surface wind speed condition—under 6 m/s (Matthews et al., 2014), the wind-stress-induced momentum can be too weak to well homogenize the upper few meters of the ocean's superficial layer, leading to stratified condition (Soloviev and Lukas, 2006). Note that after 200-km offshore, SMOS SSS bias is considerably reduced (Figure A1c).

It should be noted that the low SSS distribution in the eastern GG is less represented by ISAS SSS (Figures 1b and 1d). ISAS salinity values are always higher than the observed satellite ones, likely due to (i) the low density of in situ data (CTD/Argo) integrated into ISAS and (ii) the depth difference between salinity data measurements. Thus, studying seasonal variability freshwater plumes as well as MLS budget based on ISAS salinity product in the eastern GG would certainly introduce more uncertainties.

Appendix B: Errors Estimation

Here, the uncertainties associated with the estimation of each term in Equation 1 are presented. Data used in the present study are generally provided without an associated error estimation, except for SMOS product for which errors deduced from retrial and Bayesian method are provided along with SMOS L3 data (Boutin et al. 2018). For simplicity, in our uncertainties analysis in the seasonal cycle of each term in Equation 1, measurement errors in data set are ignored (Foltz & McPhaden, 2008). We first estimate errors for each climatological calendar month in each $0.25° \times 0.25°$ grid box. Monthly error in SSS (ϵ_S) are estimated as standard error of monthly mean SSS SMOS for each calendar month over 2010–2017. The same method is used to estimate errors in zonal current u (ϵ_u, from OSCAR), meridional current v (ϵ_v, from OSCAR) for the monthly mean of all available observations for each calendar month.

− Errors in $\partial S / \partial t$ ($\epsilon_{\partial S/\partial t}$), ZADV ($\epsilon_{ZADV}$), and MADV ($\epsilon_{MADV}$) are estimated following the formula in Flotz et al. (2008)
− Errors in SFFLUX are expressed as: $\epsilon_{SFFLUX} = (1/h)\sqrt{(\beta S/h)^2\epsilon_h^2 + S^2\epsilon_\beta^2 + \beta^2\epsilon_S^2}$ with $\beta = E - P - R$. Error in MLD (ϵ_h) is obtained from the applied objective interpolation method. Errors in E-P-R (ϵ_β) are difficult to quantify for each grid point. For the sake of simplicity, we assume that ϵ_β is homogeneous for each given study region and we estimated it as standard error of β of all grid box of the given region for each month. Given some interruptions in the run-off time-series over 2010–2017, seasonal cycle of R appears to be the main source of uncertainty for the β term

By assuming that the time series in each pair of grid boxes are uncorrelated, the monthly climatological errors for the area-averaged quantities are estimated as: $\epsilon_{\text{area-averaged}} = (1 / N) \sqrt{\sum_{i=1}^{N} \epsilon^2_i}$ where N is the number of grid boxes in a given averaging region and ϵ_i is the error for grid box i (Foltz & McPhaden, 2008).

Note that it is also tricky to estimate errors in HDIFF $(\epsilon_{\text{HDIFF}})$ and ENT (ϵ_{ENT}) for each grid point. We therefore estimated ϵ_{HDIFF} and ϵ_{ENT} as standard error of all grid boxes of the given region for each month. Note that due to the constraints of data sets (limitations and inconsistency in frequency sampling of in situ data and satellite measurement errors) and the assumption of no covariance of parameters between grid boxes, there are likely significant uncertainties associated with our estimation of errors.

Uncertainties associated with each term in Equation 1, demonstrate that our estimation of horizontal advection (both ZADV and MADV, ±0.22 pss/month), HDIFF (±0.06 pss/month), and ENT (±0.1 pss/month) are the main source of uncertainties in the MLS budget in the Niger box on average (Figure B1, top panel). Off Congo, uncertainties are mostly related to horizontal advection (of ±0.08 pss/month on average) and HDIFF (of ±0.03 pss/month) on average. During the period of development of freshwater plumes, higher uncertainties are recorded in horizontal advection of ±0.3 pss/month and ENT of about ±0.3 pss/month in the Niger box while in the Congo box uncertainties in horizontal advection are almost ±0.15 pss/month.
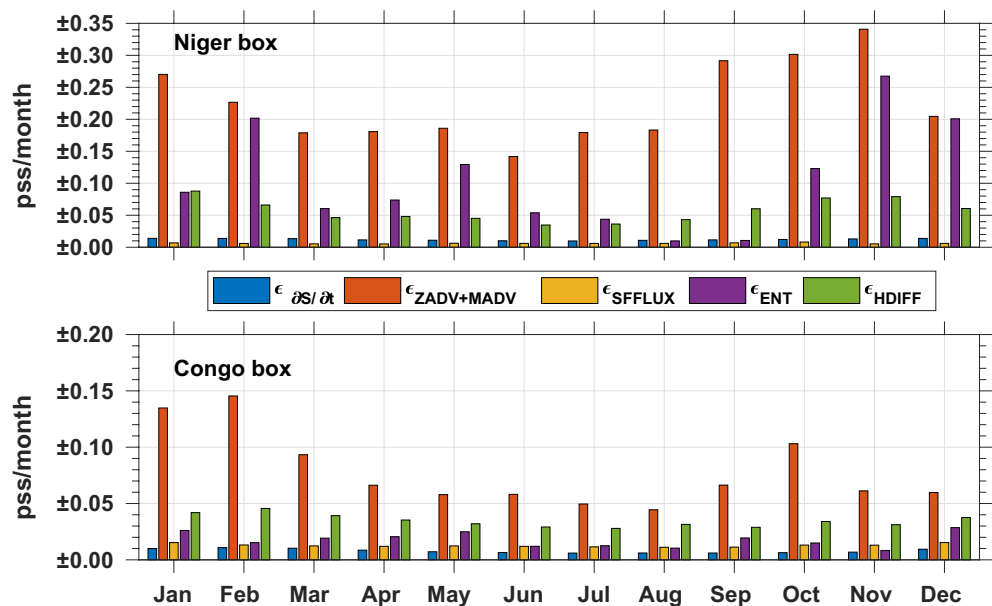

Figure B1. Errors estimated for each term int Equation 1: in the Niger box (top panel) and in the Congo box (bottom panel).

Data Availability Statement

References

Akhil, V. P., Lengaigne, M., Durand, F., Vialard, J., Chaitanya, A. V. S., Keerthi, M. G., et al. (2016). Assessment of seasonal and year-to-year surface salinity signals retrieved from SMOS and Aquarius missions in the Bay of Bengal. *International Journal of Remote Sensing*, *37*(5), 1089–1114. https://doi.org/10.1080/01431161.2016.1145362

Alory, G., Delcroix, T., Téchiné, P., Diverrès, D., Varillon, D., Cravatte, S., et al. (2015). The French contribution to the voluntary observing ships network of sea surface salinity. *Deep Sea Research Part I: Oceanographic Research Papers*, *105*(11), 1–18. https://doi.org/10.1016/j.dsr.2015.08.005

Alory, G., Maes, C., Delcroix, T., Reul, N., & Illig, S. (2012). Seasonal dynamics of sea surface salinity off Panama: The far eastern Pacific fresh pool. *Journal of Geophysical Research: Oceans*, *117*(C4). https://doi.org/10.1029/2011JC007802

Argo (2020). *Argo float data and metadata from global data assembly centre (Argo GDAC)—Snapshot of Argo GDAC as of January, 8th 2016*. SEANOE. https://doi.org/10.17882/42182

Awo, F. M., Alory, G., Da-Allada, C. Y., Delcroix, T., Jouanno, J., Kestenare, E., & Baloïtcha, E. (2018). Sea surface salinity signature of the tropical Atlantic interannual climatic modes. *Journal of Geophysical Research: Oceans*, *123*(10), 7420–7437. https://doi.org/10.1029/2018JC013837

Bakun, A. (1978). Guinea current upwelling. *Nature*, *271*(5641), 147–150. https://doi.org/10.1038/271147a0

Balaguru, K., Chang, P., Saravanan, R., Leung, L. R., Xu, Z., Li, M., & Hsieh, J.-S. (2012). Ocean barrier layers' effect on tropical cyclone intensification. *Proceedings of the National Academy of Sciences of the United States of America*, *109*(36), 14343–14347. https://doi.org/10.1073/pnas.1201364109

Bentamy, A., & Fillon, D. C. (2012). Gridded surface wind fields from Metop/ASCAT measurements. *International Journal of Remote Sensing*, *33*(6), 1729–1754. https://doi.org/10.1080/01431161.2011.600348

Berger, H., Treguier, A. M., Perenne, N., & Talandier, C. (2014). Dynamical contribution to sea surface salinity variations in the eastern Gulf of Guinea based on numerical modelling. *Climate Dynamics*, *43*(11), 3105–3122. https://doi.org/10.1007/s00382-014-2195-4

Berrit, G. R., & Donguy, J.-R. (1964). La petite saison chaude en 1959 dans la région orientale du Golfe de Guinée. *Cahiers Oceanographiques*, *16*(7–8), 657–684.

Boisvert, W. E. (1967). *Major currents in the North and South Atlantic oceans between 64°N and 60°S*. Naval Oceanographic Office. https://doi.org/10.5962/bhl.title.47773

Bourlès, B., Araujo, M., McPhaden, M. J., Brandt, P., Foltz, G. R., Lumpkin, R., et al. (2019). PIRATA: A sustained observing system for tropical Atlantic climate research and forecasting. *Earth and Space Science*, *6*(4), 577–616. https://doi.org/10.1029/2018EA000428

Bourlès, B., Herbert, G., Rousselot, P., & Grelet, J. (2018). *French PIRATA cruises S-ADCP data*. SEANOE. https://doi.org/10.17882/44635

Bourlès, B., Rousselot, P., Grelet, J., Roubaud, F., Bachelier, C., Chuchla, R., & Gouriou, Y. (2018). *French PIRATA cruises: CTD-O2 data*. SEANOE. https://doi.org/10.17882/51534

Boutin, J., Chao, Y., Asher, W. E., Delcroix, T., Drucker, R., Drushka, K., et al. (2016). Satellite and in situ salinity: Understanding near-surface stratification and subfootprint variability. *Bulletin of the American Meteorological Society*, *97*(8), 1391–1407. https://doi.org/10.1175/BAMS-D-15-00032.1

Boutin, J., Vergely, J. L., Marchand, S., D'Amico, F., Hasson, A., Kolodziejczyk, N., et al. (2018). New SMOS sea surface salinity with reduced systematic errors and improved variability. *Remote Sensing of Environment*, *214*, 115–134. https://doi.org/10.1016/j.rse.2018.05.022

Boyer, T. P., & Levitus, S. (2002). Harmonic analysis of climatological sea surface salinity. *Journal of Geophysical Research*, *107*(C12). SRF1–SRF14. https://doi.org/10.1029/2001JC000829

Brando, V. E., Braga, F., Zaggia, L., Giardino, C., Bresciani, M., Matta, E., et al. (2015). High-resolution satellite turbidity and sea surface temperature observations of river plume interactions during a significant flood event. *Ocean Science*, *11*(6), 909–920. https://doi.org/10.5194/os-11-909-2015

Brandt, P., Caniaux, G., Bourlès, B., Lazar, A., Dengler, M., Funk, A., et al. (2011). Equatorial upper-ocean dynamics and their interaction with the West African monsoon. *Atmospheric Science Letters*, *12*(1), 24–30. https://doi.org/10.1002/asl.287

Camara, I., Kolodziejczyk, N., Mignot, J., Lazar, A., & Gaye, A. T. (2015). On the seasonal variations of salinity of the tropical Atlantic mixed layer. *Journal of Geophysical Research: Oceans*, *120*(6), 4441–4462. https://doi.org/10.1002/2015JC010865

Chao, S.-Y. (1988). Wind-driven motion of estuarine plumes. *Journal of Physical Oceanography*, *18*(8), 1144–1166. https://doi.org/10.1175/1520-0485(1988)018<1144:WDMOEP>2.0.CO;2

Chao, Y., Farrara, J. D., Schumann, G., Andreadis, K. M., & Moller, D. (2015). Sea surface salinity variability in response to the Congo river discharge. *Continental Shelf Research*, *99*, 35–45. https://doi.org/10.1016/j.csr.2015.03.005

Cole, S. T., Wortham, C., Kunze, E., & Owens, W. B. (2015). Eddy stirring and horizontal diffusivity from Argo float observations: Geographic and depth variability. *Geophysical Research Letters*, *42*(10), 3989–3997. https://doi.org/10.1002/2015GL063827

Constantin, S., Doxaran, D., & Constantinescu, Ş. (2016). Estimation of water turbidity and analysis of its spatio-temporal variability in the Danube River plume (Black Sea) using MODIS satellite data. *Continental Shelf Research*, *112*, 14–30. https://doi.org/10.1016/j.csr.2015.11.009

Da-Allada, C. Y., Alory, G., Du Penhoat, Y., Kestenare, E., Durand, F., & Hounkonnou, N. M. (2013). Seasonal mixed-layer salinity balance in the tropical Atlantic Ocean: Mean state and seasonal cycle. *Journal of Geophysical Research: Oceans*, *118*(1), 332–345. https://doi.org/10.1029/2012JC008357

Da-Allada, C. Y., du Penhoat, Y., Jouanno, J., Alory, G., & Hounkonnou, N. M. (2014). Modeled mixed-layer salinity balance in the Gulf of Guinea: Seasonal and interannual variability. *Ocean Dynamics*, *64*(12), 1783–1802. https://doi.org/10.1007/s10236-014-0775-9

Da-Allada, C. Y., Jouanno, J., Gaillard, F., Kolodziejczyk, N., Maes, C., Reul, N., & Bourlès, B. (2017). Importance of the equatorial undercurrent on the sea surface salinity in the eastern equatorial Atlantic in boreal spring. *Journal of Geophysical Research: Oceans*, *122*(1), 521–538. https://doi.org/10.1002/2016JC012342

Dai, A. (2017). CISL RDA: Dai and Trenberth global river flow and continental discharge dataset. Retrieved from https://rda.ucar.edu/datasets/ds551.0

Dai, A., & Trenberth, K. E. (2002). Estimates of freshwater discharge from continents: Latitudinal and seasonal variations. *Journal of Hydrometeor*, *3*(6), 660–687. https://doi.org/10.1175/1525-7541(2002)003<0660:EOFDFC>2.0.CO;2

de Boyer Montégut, C., Durand, F., Bourdallé-Badie, R., & Blanke, B. (2014). Role of fronts in the formation of Arabian Sea barrier layers during summer monsoon. *Ocean Dynamics*, *64*(6), 809–822. https://doi.org/10.1007/s10236-014-0716-7

de Boyer Montégut, C., Madec, G., Fischer, A. S., Lazar, A., & Iudicone, D. (2004). Mixed layer depth over the global ocean: An examination of profile data and a profile-based climatology. *Journal of Geophysical Research: Oceans*, *109*(12), 1–20. https://doi.org/10.1029/2004JC002378

Dessier, A., & Donguy, J. R. (1994). The sea surface salinity in the tropical Atlantic between 10°S and 30°N-seasonal and interannual variations (1977-1989). *Deep Sea Research Part I: Oceanographic Research Papers*, *41*(1), 81–100. https://doi.org/10.1016/0967-0637(94)90027-2

Diakhaté, M., de Coëtlogon, G., Lazar, A., Wade, M., & Gaye, A. T. (2016). Intraseasonal variability of tropical Atlantic sea-surface temperature: Air-sea interaction over upwelling fronts. *Quarterly Journal of the Royal Meteorological Society*, *142*(694), 372–386. https://doi.org/10.1002/qj.2657

Djakouré, S., Penven, P., Bourlès, B., Koné, V., & Veitch, J. (2017). Respective roles of the Guinea current and local winds on the coastal upwelling in the Northern Gulf of Guinea. *Journal of Physical Oceanography*, *47*(6), 1367–1387. https://doi.org/10.1175/JPO-D-16-0126.1

Djakouré, S., Penven, P., Bourlès, B., Veitch, J., & Koné, V. (2014). Coastally trapped eddies in the north of the Gulf of Guinea. *Journal of Geophysical Research: Oceans*, *119*(10), 6805–6819. https://doi.org/10.1002/2014JC010243

Dogliotti, A. I., Ruddick, K., & Guerrero, R. (2016). Seasonal and inter-annual turbidity variability in the Río de la Plata from 15 years of MODIS: El Niño dilution effect. *Estuarine, Coastal and Shelf Science*, *182*, 27–39. https://doi.org/10.1016/j.ecss.2016.09.013

Doi, T., Tozuka, T., Sasaki, H., Masumoto, Y., & Yamagata, T. (2007). Seasonal and interannual variations of oceanic conditions in the Angola Dome. *Journal of Physical Oceanography*, *37*(11), 2698–2713. https://doi.org/10.1175/2007JPO3552.1

Dossa, A., Da-Allada, C., Herbert, G., & Bourlès, B. (2019). Seasonal cycle of the salinity barrier layer revealed in the northeastern Gulf of Guinea. *African Journal of Marine Science*, *41*(2), 163–175. https://doi.org/10.2989/1814232X.2019.1616612

Durand, F., Piecuch, C. G., Becker, M., Papa, F., Raju, S. V., Khan, J. U., & Ponte, R. M. (2019). Impact of continental freshwater runoff on coastal sea level. *Surveys in Geophysics*, *40*(6), 1437–1466. https://doi.org/10.1007/s10712-019-09536-w

Eisma, D., & Kalf, J. (1984). Dispersal of Zaire River suspended matter in the estuary and the Angola basin. *Netherlands Journal of Sea Research*, *17*(2–4), 385–411. https://doi.org/10.1016/0077-7579(84)90057-7

Eisma, D., & Van Bennekom, A. J. (1978). The Zaire River and estuary and the Zaire outflow in the Atlantic ocean. *Netherlands Journal of Sea Research*, *12*(3–4), 255–272. https://doi.org/10.1016/0077-7579(78)90030-3

Falcini, F., Khan, N. S., Macelloni, L., Horton, B. P., Lutken, C. B., McKee, K. L., et al. (2012). Linking the historic 2011 Mississippi River flood to coastal wetland sedimentation. *Nature Geoscience*, *5*(11), 803–807. https://doi.org/10.1038/ngeo1615

Foltz, G. R., Grodsky, S. A., Carton, J. A., & McPhaden, M. J. (2004). Seasonal salt budget of the northwestern tropical Atlantic Ocean along 38°W. *Journal of Geophysical Research: Oceans*, *109*(C3), 1–13. https://doi.org/10.1029/2003JC002111

Foltz, G. R., & McPhaden, M. J. (2008). Seasonal mixed layer salinity balance of the tropical North Atlantic Ocean. *Journal of Geophysical Research*, *113*(2), 1–14. https://doi.org/10.1029/2007JC004178

Foltz, G. R., & McPhaden, M. J. (2009). Impact of barrier layer thickness on SST in the central tropical North Atlantic. *Journal of Climate*, *22*(2), 285–299. https://doi.org/10.1175/2008JCLI2308.1

Fournier, S., Chapron, B., Salisbury, J., Vandemark, D., & Reul, N. (2015). Comparison of spaceborne measurements of sea surface salinity and colored detrital matter in the Amazon plume. *Journal of Geophysical Research: Oceans*, *120*, 3177–3192. https://doi.org/10.1002/2015JC010769

Fournier, S., Vialard, J., Lengaigne, M., Lee, T., Gierach, M. M., & Chaitanya, A. V. S. (2017). Modulation of the Ganges-Brahmaputra river plume by the Indian Ocean dipole and eddies inferred from satellite observations. *Journal of Geophysical Research: Oceans*, *122*(12), 9591–9604. https://doi.org/10.1002/2017JC013333

Gaillard, F., Diverres, D., Jacquin, S., Gouriou, Y., Grelet, J., Le Menn, M., et al. (2015). Sea surface temperature and salinity from French research vessels, 2001–2013. *Scientific Data*, *2*(1), 150054. https://doi.org/10.1038/sdata.2015.54

Gaillard, F., Reynaud, T., Thierry, V., Kolodziejczyk, N., & Von Schuckmann, K. (2016). In situ-based reanalysis of the global ocean temperature and salinity with ISAS: Variability of the heat content and steric height. *Journal of Climate*, *29*(4), 1305–1323. https://doi.org/10.1175/JCLI-D-15-0028.1

Geyer, W. R., Hill, P., Milligan, T., & Traykovski, P. (2000). The structure of the Eel River plume during floods. *Continental Shelf Research*, *20*(16), 2067–2093. https://doi.org/10.1016/S0278-4343(00)00063-7

Gu, G., & Adler, R. F. (2004). Seasonal evolution and variability associated with the West African monsoon system. *Journal of Climate*, *17*(17), 3364–3377. https://doi.org/10.1175/1520-0442(2004)017<3364:SEAVAW>2.0.CO;2

Hopkins, J., Lucas, M., Dufau, C., Sutton, M., Stum, J., Lauret, O., & Channelliere, C. (2013). Detection and variability of the Congo River plume from satellite derived sea surface temperature, salinity, ocean colour and sea level. *Remote Sensing of Environment*, *139*, 365–385. https://doi.org/10.1016/j.rse.2013.08.015

Horner-Devine, A. R., Hetland, R. D., & MacDonald, D. G. (2015). Mixing and transport in coastal river plumes. *Annual Review of Fluid Mechanics*, *47*(1), 569–594. https://doi.org/10.1146/annurev-fluid-010313-141408

Kang, Y., Pan, D., Bai, Y., He, X., Chen, X., Chen, C.-T. A., & Wang, D. (2013). Areas of the global major river plumes. *Acta Oceanologica Sinica*, *32*(1), 79–88. https://doi.org/10.1007/s13131-013-0269-5

Katsura, S., Oka, E., & Sato, K. (2015). Formation mechanism of barrier layer in the subtropical Pacific. *Journal of Physical Oceanography*, *45*(11), 2790–2805. https://doi.org/10.1175/JPO-D-15-0028.1

Kerr, Y. H., Waldteufel, P., Wigneron, J.-P., Delwart, S., Cabot, F., Boutin, J., et al. (2010). The SMOS mission: New tool for monitoring key elements of the global water cycle. *Proceedings of the IEEE*, *98*(5), 666–687. https://doi.org/10.1109/JPROC.2010.2043032

Köhler, J., Serra, N., Bryan, F. O., Johnson, B. K., & Stammer, D. (2018). Mechanisms of mixed-layer salinity seasonal variability in the Indian Ocean. *Journal of Geophysical Research: Oceans*, *123*(1), 466–496. https://doi.org/10.1002/2017JC013640

Kolodziejczyk, N., Boutin, J., Vergely, J.-L., Marchand, S., Martin, N., & Reverdin, G. (2016). Mitigation of systematic errors in SMOS sea surface salinity. *Remote Sensing of Environment*, *180*(7), 164–177. https://doi.org/10.1016/j.rse.2016.02.061

Kolodziejczyk, N., Diverres, D., Jacquin, S., Gouriou, Y., Grelet, J., Le Menn, M., et al. (2020). *Sea surface salinity from French RESearcH Vessels: Delayed mode dataset, annual release*. SEANOE. https://doi.org/10.17882/39475

Kolodziejczyk, N., & Gaillard, F. (2013). Variability of the heat and salt budget in the subtropical southeastern Pacific mixed layer between 2004 and 2010: Spice injection mechanism. *Journal of Physical Oceanography*, *43*(9), 1880–1898. https://doi.org/10.1175/JPO-D-13-04.1

Kolodziejczyk, N., Marin, F., Bourlès, B., Gouriou, Y., & Berger, H. (2014). Seasonal variability of the equatorial undercurrent termination and associated salinity maximum in the Gulf of Guinea. *Climate Dynamics*, *43*(11), 3025–3046. https://doi.org/10.1007/s00382-014-2107-7

Kolodziejczyk, N., Prigent-Mazella, A., & Gaillard, F. (2017). *ISAS15 temperature and salinity gridded fields*. SEANOE. https://doi.org/10.17882/52367

Kopte, R. (2016). The Angola current: Flow and hydrographic characteristics as observed at 11°S. *Journal of Geophysical Research: Oceans*, *122*, 1–15. https://doi.org/10.1002/2016JC012374

Lagerloef, G. S. E. (2002). Introduction to the special section: The role of surface salinity on upper ocean dynamics, air-sea interaction and climate. *Journal of Geophysical Research: Oceans*, *107*(C12), SRF1–SRF2. https://doi.org/10.1029/2002JC001669

Lagerloef, G. S. E., Mitchum, G. T., Lukas, R. B., & Niiler, P. P. (1999). Tropical Pacific near-surface currents estimated from altimeter, wind, and drifter data. *Journal of Geophysical Research*, *104*(C10), 23313–23326. https://doi.org/10.1029/1999JC900197

Lass, H. U., & Mohrholz, V. (2008). On the interaction between the subtropical gyre and the subtropical cell on the shelf of the SE Atlantic. *Journal of Marine Systems*, *74*(1–2), 1–43. https://doi.org/10.1016/j.jmarsys.2007.09.008

Laurindo, L. C., Mariano, A. J., & Lumpkin, R. (2017). An improved near-surface velocity climatology for the global ocean from drifter observations. *Deep Sea Research Part I: Oceanographic Research Papers*, *124*, 73–92. https://doi.org/10.1016/j.dsr.2017.04.009

Lemasson, L., & Rebert, J.-P. (1973). Les courants marins dans le Golfe Ivoirien. *Cahiers ORSTOM*, *XI*(1), 67–95.

Maes, C., & O'Kane, T. J. (2014). Seasonal variations of the upper ocean salinity stratification in the Tropics. *Journal of Geophysical Research: Oceans*, *119*(3), 1706–1722. https://doi.org/10.1002/2013JC009366

Mahé, G. (1991). La variabilité des apports fluviaux au golfe de Guinée utilisée comme indice climatique. In C. Philippe, & R. Claude (Eds.), *Pêcheries Ouest Africaines: Variabilité, Instabilité et Changement* (pp. 147–161). Orstom. Retrieved from http://www.documentation.ird.fr/hor/fdi:36287

Mahé, G., & Olivry, J.-C. (1999). Assessment of freshwater yields to the ocean along the intertropical Atlantic coast of Africa (1951–1989). *Comptes Rendus de l'Academie des Sciences - Series IIA: Earth and Planetary Science*, *328*(9), 621–626. https://doi.org/10.1016/S1251-8050(99)80159-1

Marié, L., Collard, F., Nouguier, F., Pineau-Guillou, L., Hauser, D., Boy, F., et al. (2020). Measuring ocean total surface current velocity with the KuROS and KaRADOC airborne near-nadir Doppler radars: A multi-scale analysis in preparation for the SKIM mission. *Ocean Science*, *16*(6), 1399–1429. https://doi.org/10.5194/os-16-1399-2020

Materia, S., Gualdi, S., Navarra, A., & Terray, L. (2012). The effect of Congo River freshwater discharge on Eastern Equatorial Atlantic climate variability. *Climate Dynamics*, *39*, 2109–2125. https://doi.org/10.1007/s00382-012-1514-x

Matthews, A. J., Baranowski, D. B., Heywood, K. J., Flatau, P. J., & Schmidtko, S. (2014). The surface diurnal warm layer in the Indian Ocean during CINDY/DYNAMO. *Journal of Climate*, *27*(24), 9101–9122. https://doi.org/10.1175/JCLI-D-14-00222.1

Mecklenburg, S., Drusch, M., Kerr, Y. H., Font, J., Martin-Neira, M., Delwart, S., et al. (2012). ESA's soil moisture and ocean salinity mission: Mission performance and operations. *IEEE Transactions on Geoscience and Remote Sensing*, *50*(5), 1354–1366. https://doi.org/10.1109/TGRS.2012.2187666

Meulenbergh, J. (1968). Diffusion des eaux du fleuve Congo dans les eaux de l'Atlantique Sud. Mémoires de La Classe Des Sciences Techniques. *(N.S.) ARSOM. 1968 T. XVI , f. 6: 148 (in-8°)*.

Mignot, J., de Boyer Montégut, C., Lazar, A., & Cravatte, S. (2007). Control of salinity on the mixed layer depth in the world ocean: 2. Tropical areas. *Journal of Geophysical Research*, *112*(C10), C10010. https://doi.org/10.1029/2006JC003954

Mignot, J., de Boyer Montégut, C., & Tomczak, M. (2009). On the porosity of barrier layers. *Ocean Science*, *5*(3), 379–387. https://doi.org/10.5194/os-5-379-2009

Mignot, J., Lazar, A., & Lacarra, M. (2012). On the formation of barrier layers and associated vertical temperature inversions: A focus on the Northwestern tropical Atlantic. *Journal of Geophysical Research: Oceans*, *117*(2), 1–11. https://doi.org/10.1029/2011JC007435

Moisan, J. R., & Niiler, P. P. (1998). The seasonal heat budget of the North Pacific: Net heat flux and heat storage rates (1950-1990). *Journal of Physical Oceanography*, *28*(3), 401–421. https://doi.org/10.1175/1520-0485(1998)028<0401:TSHBOT>2.0.CO;2

Ollitrault, M., & Rannou, J.-P. (2013). ANDRO: An Argo-based deep displacement dataset. *Journal of Atmospheric and Oceanic Technology*, *30*(4), 759–788. https://doi.org/10.1175/JTECH-D-12-00073.1

Pailler, K., Bourlès, B., & Gouriou, Y. (1999). The barrier layer in the western tropical Atlantic Ocean. *Geophysical Research Letters*, *26*(14), 2069–2072. https://doi.org/10.1029/1999gl900492

Ren, L., & Riser, S. C. (2009). Seasonal salt budget in the northeast Pacific ocean. *Journal of Geophysical Research*, *114*(12), 1–11. https://doi.org/10.1029/2009JC005307

Ren, L., Speer, K., & Chassignet, E. P. (2011). The mixed layer salinity budget and sea ice in the Southern Ocean. *Journal of Geophysical Research*, *116*(C8), C08031. https://doi.org/10.1029/2010JC006634

Reul, N., Fournier, S., Boutin, J., Hernandez, O., Maes, C., Chapron, B., et al. (2014). Sea surface salinity observations from space with the SMOS satellite: A new means to monitor the marine branch of the water cycle. *Surveys in Geophysics*, *35*(3), 681–722. https://doi.org/10.1007/s10712-013-9244-0

Reul, N., Grodsky, S. A., Arias, M., Boutin, J., Catany, R., Chapron Bertrand, D. 'A. F., et al. (2020). Sea surface salinity estimates from spaceborne L-band radiometers: An overview of the first decade of observation (2010–2019) . *Remote Sensing of Environment*, *242*(37), 111769. https://doi.org/10.1016/j.rse.2020.111769

Reul, N., Quilfen, Y., Chapron, B., Fournier, S., Kudryavtsev, V., & Sabia, R. (2014). Multisensor observations of the Amazon-Orinoco river plume interactions with hurricanes. *Journal of Geophysical Research: Oceans*, *119*, 8271–8295. https://doi.org/10.1002/2014JC010107

Reverdin, G., Kestenare, E., Frankignoul, C., & Delcroix, T. (2007). Surface salinity in the Atlantic Ocean (30°S–50°N). *Progress in Oceanography*, *73*(3–4), 311–340. https://doi.org/10.1016/j.pocean.2006.11.004

Richardson, P. L., & Reverdin, G. (1987). Seasonal cycle of velocity in the Atlantic North Equatorial Countercurrent as measured by surface drifters, current meters, and ship drifts. *Journal of Geophysical Research*, *92*(C4), 3691. https://doi.org/10.1029/JC092iC04p03691

Riser, S. C., Freeland, H. J., Roemmich, D., Wijffels, S., Troisi, A., Belbéoch, M., et al. (2016). Fifteen years of ocean observations with the global Argo array. *Nature Climate Change*, *6*(2), 145–153. https://doi.org/10.1038/nclimate2872

Scannell, H. A., & McPhaden, M. J. (2018). Seasonal mixed layer temperature balance in the Southeastern tropical Atlantic. *Journal of Geophysical Research: Oceans*, *123*(8), 5557–5570. https://doi.org/10.1029/2018JC014099

Schlundt, M., Brandt, P., Dengler, M., Hummels, R., Fischer, T., Bumke, K., et al. (2014). Mixed layer heat and salinity budgets during the onset of the 2011 Atlantic cold tongue. *Journal of Geophysical Research: Oceans*, *119*(11), 7882–7910. https://doi.org/10.1002/2014JC010021

Schroeder, T., Devlin, M. J., Brando, V. E., Dekker, A. G., Brodie, J. E., Clementson, L. A., & McKinna, L. (2012). Inter-annual variability of wet season freshwater plume extent into the Great Barrier Reef lagoon based on satellite coastal ocean colour observations. *Marine Pollution Bulletin*, *65*(4–9), 210–223. https://doi.org/10.1016/j.marpolbul.2012.02.022

Soloviev, A., & Lukas, R. (2006). *The near-surface layer of the ocean: Structure, dynamics and applications*. Springer. https://doi.org/10.1007/1-4020-4053-9

Soloviev, A., Lukas, R., & Matsuura, H. (2002). Sharp frontal interfaces in the near-surface layer of the tropical ocean. *Journal of Marine Systems*, *37*(1–3), 47–68. https://doi.org/10.1016/S0924-7963(02)00195-1

Sprintall, J., & Tomczak, M. (1992). Evidence of the barrier layer in the surface layer of the tropics. *Journal of Geophysical Research*, *97*(C5), 7305. https://doi.org/10.1029/92jc00407

Sudre, J., Maes, C., & Garçon, V. (2013). On the global estimates of geostrophic and Ekman surface currents. *Limnology & Oceanography*, *3*(1), 1–20. https://doi.org/10.1215/21573689-2071927

Talley, L. D., Pickard, G. L., Emery, W. J., & Swift, J. H. (2011). *Descriptive physical oceanography: An introduction* (6th ed.). Elsevier Ltd.

Thanh, V. Q., Roelvink, D., van der Wegen, M., Reyns, J., Kernkamp, H., Van Vinh, G., & Linh, V. T. P. (2020). Flooding in the Mekong Delta: The impact of dyke systems on downstream hydrodynamics. *Hydrology and Earth System Sciences*, *24*(1), 189–212. https://doi.org/10.5194/hess-24-189-2020

Tzortzi, E., Josey, S. A., Srokosz, M., & Gommenginger, C. (2013). Tropical Atlantic salinity variability: New insights from SMOS. *Geophysical Research Letters*, *40*(10), 2143–2147. https://doi.org/10.1002/grl.50225

Varona, H. L., Veleda, D., Silva, M., Cintra, M., & Araujo, M. (2019). Amazon River plume influence on Western Tropical Atlantic dynamic variability. *Dynamics of Atmospheres and Oceans*, *85*, 1–15. https://doi.org/10.1016/j.dynatmoce.2018.10.002

Vialard, J., Menkes, C., Boulanger, J.-P., Delecluse, P., Guilyardi, E., McPhaden, M. J., & Madec, G. (2001). A model study of oceanic mechanisms affecting equatorial pacific sea surface temperature during the 1997-98 El Niño. *Journal of Physical Oceanography*, *31*(7), 1649–1675. https://doi.org/10.1175/1520-0485(2001)031<1649:AMSOOM>2.0.CO;2

Vic, C., Berger, H., Tréguier, A.-M., & Couvelard, X. (2014). Dynamics of an equatorial river plume: Theory and numerical experiments applied to the Congo plume case. *Journal of Physical Oceanography*, *44*(3), 980–994. https://doi.org/10.1175/JPO-D-13-0132.1

Vieira, L. H., Krisch, S., Hopwood, M. J., Beck, A. J., Scholten, J., Liebetrau, V., & Achterberg, E. P. (2020). Unprecedented Fe delivery from the Congo River margin to the South Atlantic Gyre. *Nature Communications*, *11*(1), 556. https://doi.org/10.1038/s41467-019-14255-2

Wade, M., Caniaux, G., & du Penhoat, Y. (2011). Variability of the mixed layer heat budget in the eastern equatorial Atlantic during 2005–2007 as inferred using Argo floats. *Journal of Geophysical Research*, *116*(C8), C08006. https://doi.org/10.1029/2010JC006683

Wauthy, B. (1977). Révision de la Classification des eaux de surface du Golfe De Guinée (BERRIT 1961). *Cahiers ORSTOM. Série Océanographie*, *15*(3), 279–295.

Yu, L. (2011). A global relationship between the ocean water cycle and near-surface salinity. *Journal of Geophysical Research*, *116*(C10), C10025. https://doi.org/10.1029/2010JC006937